Joint Estimation of Leaf Area Density and Leaf Angle Distribution Using TLS Point Cloud for Forest Stands

Ameni Mkaouar, Abdelaziz Kallel, Zouhaier Ben Rabah, and Thouraya Sahli Chahed

***Abstract*—The foliage density (u_l) and the leaf angle distribution (LAD) are important properties that impact radiation transmission, interception, absorption and, therefore, photosynthesis. Their estimation in a forested scene is a challenging task due to their interdependence in addition to the large variability in the forest structure and the heterogeneity of the vegetation. In this work, we propose to jointly estimate both of them using terrestrial laser scanner (TLS) point cloud for different forest stands. Our approach is based on direct/inverse radiative transfer modeling. The direct model was developed to simulate TLS shots within a vegetation scene having known foliage properties (i.e., u_l and LAD) resulting in a 3-D point cloud of the observed scene. Then, the inverse model was developed to jointly estimate u_l and LAD decomposing the 3-D point cloud into voxels. The problem turns out to a high-dimensional cost function to optimize. To do it, the shuffled complex evolution method has been adopted. Our approach is validated with results derived from several simulated homogeneous and heterogeneous vegetation canopies as well as from actual TLS point cloud acquired from Estonian Birch, Pine, and Spruce stands. Our findings revealed that our estimates were considerably close to the actual u_l and leaf inclination distribution function (LIDF) values with ($\text{Biais}_{u_l} \in [0.001\ 0.006]$, $\text{RMSE}_{u_l} \in [0.019\ 0.045]$, $\text{RMSE}_{\text{LIDF}} \in [0.019\ 0.038]$) for homogeneous dataset and ($\text{Biais}_{u_l} \in [0.001\ 0.045]$, $\text{RMSE}_{u_l} \in [0.023\ 0.078]$, $\text{RMSE}_{\text{LIDF}} \in [0.011\ 0.018]$) for heterogeneous dataset with different tree crown geometries (i.e., conical and elliptical). In the actual case (Birch, Pine, and Spruce stands), our approach with the traditional and novel techniques, RMSE_{LAI} are 0.526 and 0.105, respectively. The results outperform those of the baseline technique (i.e., assuming spherical LAD) with $\text{RMSE}_{\text{LAI}} = 2.651$.**

Manuscript received March 16, 2021; revised June 9, 2021 and October 6, 2021; accepted October 9, 2021. Date of publication October 15, 2021; date of current version November 11, 2021. This work was supported in part by the INFOTEL-3 project led by the National Center for Mapping and Remote Sensing, Tunisia. This work is carried out under the MOBIDOC scheme, funded by the EU through the Emori Program and managed by the National Agency for the Promotion of Scientific Research. *(Corresponding author: Ameni Mkaouar.)*

Ameni Mkaouar is with the Signals, Systems Artificial Intelligence, and Networks (SM@RTS), Centre de recherche en numerique de Sfax (CRNS), University of Sfax, Sfax technopole, Sfax 3021, Tunisia, and also with the National School of Engineering of Sfax (ENIS), University of Sfax, Sfax 3029, Tunisia (e-mail: ameni.mkaouar93@gmail.com).

Abdelaziz Kallel is with the Signals, Systems Artificial Intelligence, and Networks (SM@RTS), Centre de recherche en numerique de Sfax, University of Sfax, Sfax 3021, Tunisia (e-mail: abdelaziz.kallel@crns.rnrt.tn).

Zouhaier Ben Rabah is with the National School of Computer Science, SIVIT-RIADI Laboratory, University of Manouba, Manouba 2010, Tunisia, and also with the National Center for Mapping and Remote Sensing, Ministry of National Defense, Tunis 1080, Tunisia (e-mail: zouhaierbr@yahoo.fr).

Thouraya Sahli Chahed is with the National Center for Mapping and Remote Sensing, Ministry of National Defense, Tunis 1080, Tunisia (e-mail: t_sahli@yahoo.fr).

Digital Object Identifier 10.1109/JSTARS.2021.3120521

***Index Terms*—Leaf angle distribution (LAD), leaf area density, leaf area index (LAI), leaf properties, TLS, voxel-based method.**

I. Introduction

THE forest ecosystem plays an essential role in our planet as it maintains climate, protects biodiversity, and provides oxygen through the global impact of photosynthesis [1]. Developing effective strategies to promote sustainable forest management and development is needed and it requires a comprehensive study of the 3-D forest structure. Researchers on forestry introduced a list of different biophysical and biochemical properties [2], [3] to inspect and understand plants structure and behavior and to assess vegetation physiological conditions (e.g., photosynthesis and evapotranspiration). For instance, leaf area index (LAI), foliage density (u_l), and leaf angle distribution (LAD) are key properties of vegetation structure. They control the fraction of absorbed photosynthetically active radiation and consequently the photosynthesis activity [4], [5]. During the past decades, many studies have examined the problem of biophysical foliage properties retrieval using different methods and based on different theories in either local or regional scale. These methods are classified as direct and indirect. Direct methods, also known as traditional measurements, serve generally as the ground truth of the assessed parameters. They provide direct access to the leaf surface and orientation based on a given sampling method, i.e., only a proportion of the population is inspected and inferences regarding the whole population are based on this sample. However, these manual methods are destructive, labor-intensive, and highly time consuming [6], [7]. Moreover, these methods do not allow practical canopy investigation for forests where the access is almost blocked by trees and understories.

To overcome this issue indirect methods based on remote sensing (RS) were developed to fill this gap of mapping forests and retrieving their properties in a systematic way [8], [9]. It allows us to access the foliage structure by analyzing radiation interception inside the vegetation canopy. RS was applied to forestry using imagery or laser scanning to assess its resources [10]. Most laser scanning applications that are developed for forestry use aerial systems (ALS) as this method of acquisition is suitable for large areas [11], [12]. However, to collect tree-level or stand-level field data, terrestrial laser scanner (TLS), mobile laser scanner (MLS), and/or backpack laser scanner show a promising potential [13]–[15]. In [16], for example, MLS data were utilized in urban tree inventories to demonstrate the feasibility of extracting geometrical forest information. However,

unlike the TLS, the MLS is more convenient to be used in urban areas as the sensor can be fixed to a vehicle.

The aforementioned LiDAR systems scan the observed scene by sending laser pulses toward the target then they record both time and the back-scattered energy allowing them to compute distance from the emitter to the detected object resulting on a 3-D representation of the scene. Their high accuracy and resolution allow the scanning of the 3-D structural details of the vegetation with precision lower than 1 cm.

TLS has proven to be able to provide detailed information on the canopy attributes. Particularly, it permits automatic detection of stem positions and tree stem dimensions with high precision in different stands [17]. In [18], it was used to evaluate the 3-D plant area index. In [19], TLS data were exploited to improve the LAI estimated by correcting the clumping and woody effects. Multiple other works were also performed to investigate the overall canopy. Although TLS is widely being used to derive canopy structure, its application for LAD and u_l derivation remains limited [20].

Several attempts have already been made to measure LAI/u_l and LAD using TLS instruments. In general, LAI/u_l are estimated from TLS point cloud by either geometrical or statistical modeling. In [21], LAI was estimated over tropical forests from TLS point cloud proposing an algorithmic approach named point spatial density algorithm. The proposed method involves filtering and 3-D reconstruction of individual trees. Individual tree reconstruction in this case requires a dense point cloud. Such techniques does not take advantage from the TLS long-range measurements since in this case, trees could be occluded by others which are in front of the sensor. Estimating LAI from such a limited number of reconstructed trees may not be significant for the entire forest stand, and accuracy may be affected. A community of researchers improved LAI/u_l estimation. Their developments are centered on the clumping index, gap size distribution, and crown gap probabilities [22], [23]. In such cases, LAI is calculated using a 3-D method, which requires direct manipulation of large point cloud data. LAI/u_l was analyzed using voxels in another work [18], where a sensitivity analysis was conducted on affecting parameters relevant to geometrical and structural variables. In this case, when the method was applied to realistic tree models, the accuracy of the vegetation density estimates was reduced by clumping effects and the presence of woody elements. An important family of methods developed to estimate LAI/u_l uses mathematical generalizations derived from the Beer–Lambert law [24]. In such an approach, the decrease in radiation through a vegetation layer is assessed to compute LAI/u_l of this layer from vegetation transmittance which requires knowledge of leaf orientation within the canopy. If not $a\ priori$ known, a simplified distribution (e.g., spherical LAD) is generally adopted but this may introduce significant errors in LAI/u_l retrieval [25].

Furthermore, some efforts have also been made to assess the LAD. In [26], LAD were estimated from clustered point cloud in each voxel by deriving the cluster normal distribution. However, a possible source of error is that adjacent clustered points may not be on the same leaf. In [27], it was also proposed to use normal vectors to estimate the leaf angle that is calculated from a subset of points. The latter method was able, for maple and sugar trees, to predict the leaf inclination with R^2 of 0.73 and 0.573, respectively. However, the proposed approach is only validated with individual trees, thus, for a reduced volume of TLS point cloud. In [28], there is another example of approach to extract leaf point and to reconstruct leaf surface to be able to calculate leaf normal vectors, thus, LAD from TLS. However, in this case, wrongly classified woody points as leaf points affect LAD retrieval and it requires dense TLS point cloud, and therefor, it cannot efficiently use long-range TLS.

To sum up, in several research works practical u_l and LAD estimation methods using TLS data have been proposed. Although all these methods showed potential but in general, u_l and LAD measurement using TLS data is facing multiple challenges. For instance, they are susceptible to misclassification between woody and leaf point clouds or limited to individual tree reconstruction. Furthermore, they are affected by point cloud density. It is worth noting that using a low-density point cloud or dealing with stand far from the sensor will affect the precision of the results. As far as we know, state of the art works were not dealing with such challenges, the decrease of the point cloud density when using long-range TLS has not been yet tested to jointly estimate u_l and LAD and their potential to limit estimation accuracy remains questionable.

In this study, we propose to tackle the problem of joint estimation of u_l and LAD using TLS point cloud for large scenes. The novelty of our approach is the introduction of a new way to jointly retrieve u_l and LAD rather than use LAD assumptions as before [29]. For that reason, we propose an original approach based on radiative transfer direct and inverse modeling. The direct one allows us to simulate TLS measurements with different complexity level. Whereas, the inverse model tries to retrieve the vegetation properties given the observation. We propose two different techniques (traditional and novel). The difference between them is the way how to process the path length inside each voxel to deal with the low-density point cloud issue.

II. Theoretical Background

Methods of u_l retrieval are based on the measurement of the radiation transmittance through the canopy as first introduced in [24]. u_l and canopy transmittance T are linked according to the Beer–Lambert law that expresses T of radiation across a vegetation layer considering the foliage element distribution as

$$T(\theta) = \exp(-G_{\mathrm{LAD}}(\theta).u_l.\overline{\Delta l}(\theta)) \tag{1}$$

where θ is the radiation zenith angle, $\overline{\Delta l}$ is the path-length through the vegetation layer, and G_{LAD}, commonly known as the G-function, defined as the projection coefficient of the leaf area on the plane perpendicular to the viewing direction [30], and it is function of the LAD. The value of G could be computed by averaging the scalar product between the propagation direction $\widehat{n}$ and the leaf normal, $\widehat{n}_l(\theta_l, \varphi_l)$, over the leaf inclination angle distribution as seen in the following equation:

$$G_{\mathrm{LAD}}(\theta) = \int_0^{2\pi} \int_0^{\pi/2} \frac{1}{2\pi} |\widehat{n}.\widehat{n}_l| f(\theta_l) \mathrm{d}\theta_l \mathrm{d}\varphi_l \tag{2}$$

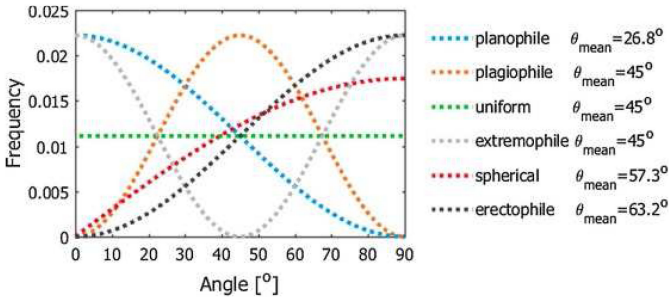

Fig. 1. Six archetype functions used to approximate LAD and the corresponding mean angle of orientation [28].

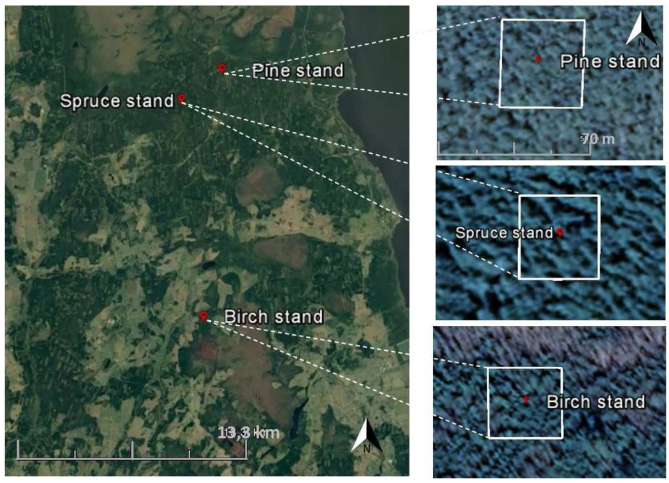

Fig. 2. Järvselja forest in Estonia. The white squares correspond to the Pine, Spruce, and Birch stands. They are of dimension $(100\text{ m} \times 100\text{ m})$ centered at $(58°18'40.90''N, 27°17'48.40''E)$, $(58°17'43.0''N, 27°15'22.0''E)$, and $(58°10'49.81''N, 27.°19'51.53''E)$, respectively.

where $f(\theta_l)$ is the leaf inclination distribution function (LIDF), a mathematical description of LAD.

Due to measurement challenges and complexity, LAD is sometimes simplified using predefined mathematical functions. Fig. 1 illustrates examples of commonly used LIDF. They are parametrized by the average leaf angle, θ_{mean} [28]. For instance, the spherical distribution is characterized by a constant value over all the possible angles and for which $\theta_{\text{mean}} = 57.3°$. In this case, the corresponding G-function is always 0.5 in any viewing direction. Even though such distribution is largely used [29], it does not always fit the reality [25]. Two extreme distributions characterized by small and large inclination angles, they are the planophile and the erectophile distributions, respectively. Noteworthy, in our inversion technique, we do not use any parameterization of the LIDF to be more flexible.

III. Study Site and TLS Measurements

A. Study Site

The study area is a forest site located in Järvselja, Estonia $(58.3°N, 27.3°E)$. Three $(100\text{ m} \times 100\text{ m})$ mature forest stands are selected as a study plots, as shown in Fig. 2. In 2007, a comprehensive inventory of the tree level was performed in the stands. Järvselja forests are located on a flat landscape at 50 m above sea level, i.e., when analyzing TLS data, there are no topographic influences that need to be taken into consideration. Table I provides a general overview of the stands considered in this work.

TABLE I
Description of the Three Studied Forest Stands in the Järvselja Database [31], [32]

Stand	Age	N	H	LAI_{all}
Birch	49	992	27	3.93
Pine	124	1122	16	1.86
Spruce	59	1689	23	4.36

Age—Stand Age in Years; N—Number of trees in the 1 Ha Stand; H—Dominant species height in metres; LAI_{all}—Allometric LAI.

TABLE II
Specifications of the Leica ScanStation C10 Laser Scanner

Parameters	Characteristics/Value
Horizontal scanning	up to 360°
Vertical scanning	up to 270°
Laser wavelength	$532nm$

Birch stand is dominated by Birch (*Betula pendula*) 57%, Common alder (*Alnus glutinosa*) 29.5%, and Aspen (*Populus tremula*) 11%, the total number of trees per hectare is 992.

Pine (*Pinus sylvestris*) stand grows on the transitional bog. In 2018, the stand height is 15.6 m, the stand is 124 years old, and stand density is 1122 trees per hectare.

Spruce (*Picea abies*) stand grows on a *Gleyi Ferric Podzol* site. Stand age is 59 years. Two tree layers can be distinguished according to the social status of the trees. There is an average height of 23.2 m in the first (upper) layer with 774 trees per hectare and 915 trees per hectare in the second where the height of trees ranges from 3.5 to 20 m. A more detailed description of the test site was provided in [31].

B. TLS Measurements

TLS data were acquired using Leica ScanStation C10 laser scanner on 2013. Table II shows the TLS properties. The resolution of the TLS was fixed to 0.08 m × 0.08 m at the 100 m distance on a perpendicular surface. Since the scanner radially spreads out its shots, the point cloud can be as dense as 4 m × 4 m from its position at a distance of 5 m.

The developed method is validated using TLS point cloud from three stands of dimension $(100\text{ m} \times 100\text{ m})$. TLS measurements were taken at different positions, as shown in [32]. In this study, we used data acquired at the center of each stand.

It is important to notice that even though the TLS acquisitions and the forestry measurements of the stands are separated by years, the validation remains possible. Indeed, the stands, (e.g., Pine stand age is 124 years), are mature, and changes in stand structure are slow [31] for that reason LAI estimation validation is possible [23].

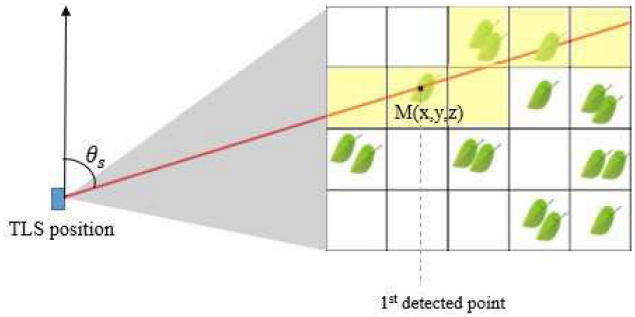

Fig. 3. Simulation of laser beam path inside a voxelized vegetation scene. TLS ray intercept a leaf at position $M(x, y, z)$.

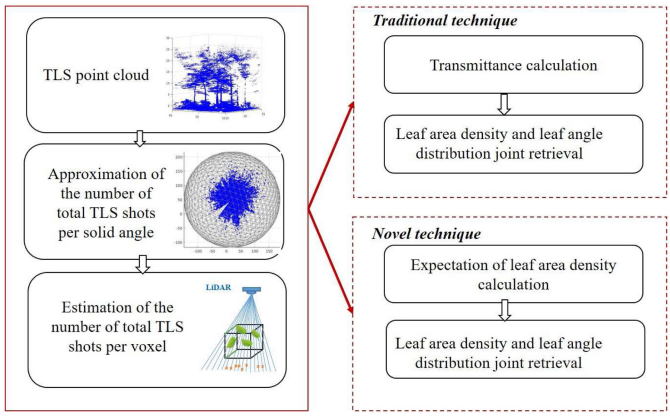

Fig. 4. Flowchart of the leaf area density (u_l) and the LAD estimation using TLS point cloud.

IV. Methodology

The aim of this work is to derive the structural foliage properties (u_l and LAD) from TLS point cloud. Our approach was developed and validated using both actual and simulated TLS data. The use of simulated data was essential for a comprehensive understanding of the interaction between forest components and laser pulses aiding on mastering how instrumental parameters and plants properties affects final results. However, no parameterization expect the voxel size is required to be optimized on simulations to be used after that in actual data processing.

Our methodology consists of the following two parts: (i) the generation of 3-D point cloud from simulated TLS observations within different vegetation scenes and (ii) the estimation of foliage parameters using both simulated and actual TLS point clouds.

A. Direct Model for Scene Creation and TLS Data Generation

The use of simulated data was chosen to evaluate u_l and LAD in a reliable, managed, and systematic manner, particularly because the simulation framework relies on an accurate ray tracing algorithm to produce the TLS point cloud for the vegetation scene being observed. Our proposed model is composed of two tasks. First, creating a vegetation scene which represents the mock-ups scanned by the sensor. Here, two distinct types of mock-ups are used: initially, a homogeneous vegetation plot known as a foliage canopy layer, which is used as a vegetation volume composed of leaves randomly distributed according to known u_l and LAD values. Then, a heterogeneous forest scene was established, with spaced trees having as well a known u_l and LAD values. For simplicity sake, trees were simulated as cones and ellipses (e.g., coniferous trees).

Second, simulating the laser beams lunched inside the scene to build a 3-D point cloud. The TLS orientation is varied in a way that it covers the entire mock-up. Its angular variations was regularly sampled over zenithal and azimuthal angles.

The intersection was checked with each beam, as shown in Fig. 3, in a simulated TLS scan with leaves inside the canopy based on a ray tracing technique that maps the laser shot path inside the created scene voxel by voxel and detects the first interception with leaf. The result of this scanning is a 3-D point cloud of the intercepted shots.

B. Inverse Model for Foliage Structure Properties Retrieval

To assess u_l and LAD precisely and accurately, we develop an approach based on solving (1) at voxel level. A new resolution technique is proposed in this context. In Fig. 4, a traditional resolution technique is also shown in order to explain how it is possible to integrate it in our work-flow and then to be compared with the new technique. In this work, the TLS point cloud is divided up into voxels within them u_l is estimated. The latter task requires the transmittance calculation in each voxel which in terns depends on the percentage of rays that exit the voxel without interception. The latter requires a prior knowledge of the total number of TLS shots inside each voxel $N_{\text{vox}}^{\text{tot}}$. $N_{\text{vox}}^{\text{tot}}$ derivation from TLS data is considered as an ill-posed problem. In fact, the emitted rays from the sensor are not totally intercepted, there are some rays, which are escaped without any contact. Neglecting the latter in $N_{\text{vox}}^{\text{tot}}$ derivation leads to an overestimation, and therefore, a bias in u_l assessment.

The combination of vegetation structure variability and shooting pattern of TLS scanner effects leads to a highly heterogeneous spatial distribution point cloud. This increases the complexity of the estimation of the number of total TLS shots at voxel scale. Therefore, to around uncertainty issue, shots number is derived first over a tessellation of the hemisphere around the sensor, in which regularization hypothesis can be assumed.

1) Derivation of the Number of Total TLS Shots: Due to the occlusion effect, the number of TLS shots per solid angle, and hence, the number of intercepted ones, decrease exponentially as a function of distance from the sensor (1). Actually, close objects block the sensor view that explains the larger density of point cloud at near distances than far ones but that does not prevent that there are some escaped shots. Moreover, the size of the TLS footprint is very small (does not exceed 3 m at a distance of 20 m) in comparison to the leaf size (e.g., Birch leaf area $= 20.7$ cm^2), allowing us to ignore the multiecho effect. Therefore, it is possible to parametrize the number of intercepted shots decrease as a function of the distance, and so it is possible to extrapolate the interception outside the canopy, and therefore, it will be possible to approximate the sum of all the intercepted shots if the vegetation layer has infinite size. Moreover, in this

case, all the rays are intercepted and the found number is no other than the total number of shots per solid angle ($\Delta\Omega$), $N_{\text{tot}}^{\Delta\Omega}$. Unfortunately, in practical such method produces inaccurate results since the vegetation is not homogeneous and the number of interception decrease do not fit the exponential form.

To overcome this problem and decrease the noise, we need to average this interception over a large number of solid angles. For that reason, we take as assumption that the number of shots is almost the same for a given zenith angle, i.e., the sensor emits the same amount of rays in all azimuth directions and this emission can be only variable as a function of the zenith angle. The number of rays, $N_{\text{tot}}^{\Delta\theta}$, per zenith angle, $\Delta\theta$, is then estimated as the sum of the number of interceptions over the distance r from 0 to infinity. Let $N_{\text{itcp}}^{\Delta\theta}(r,\Delta r)$ be the number of interceptions in the distance interval $[r, r+\Delta r]$; therefore, one can write

$$\begin{aligned} N_{\text{tot}}^{\Delta\theta} &= \textstyle\sum_{r=0,\Delta r,2\Delta r,\ldots} N_{\text{itcp}}^{\Delta\theta}(r,\Delta r) \\ &= \textstyle\sum_{r=0,\Delta r,2\Delta r,\ldots} \frac{N_{\text{itcp}}^{\Delta\theta}(r,\Delta r)}{\Delta r}\Delta r \\ &= \int_{r=0}^{+\infty} \underbrace{\frac{\mathrm{d}N_{\text{itcp}}^{\Delta\theta}(r)}{\mathrm{d}r}}_{n_{\text{itcp}}^{\Delta\theta}(r)} \mathrm{d}r \end{aligned} \tag{3}$$

where $n_{\text{itcp}}^{\Delta\theta}(r)$ is the density of interception number.

As explained at the beginning of this section, $n_{\text{itcp}}^{\Delta\theta}(r)$ is an exponentially decreasing function given by

$$n_{\text{itcp}}^{\Delta\theta}(r) = A\exp(-\alpha\times r) \tag{4}$$

where A and α are two parameters to estimate from the data.

Note that, for homogeneous vegetation layer of constant density u_l, $\alpha = G(\Delta\theta).u_l$.

Therefore, one obtains from (3) and (4)

$$N_{\text{tot}}^{\Delta\theta} = \int_{r=0}^{+\infty} A\exp(-\alpha\times r)\mathrm{d}r = \frac{A}{\alpha}. \tag{5}$$

In practical point of view, solid angle generation is performed by triangulating the spherical surface surrounding the point cloud into triangles having almost the same size, where the sensor position is considered as the sphere center that allows us to produce solid angles originated from the sensor to each triangle vertices. Then, as already said, to ease the computation process and to avoid problems caused by the heterogeneity, all solid angles were clustered by subdividing the zenith angle θ_s per 10° step, $\{\Delta\theta_i\}_{i=1,\ldots,9}$. The choice of 10° was a compromise between the reliable variation in the number of detected points and the accuracy of the results.

Each solid angle belongs to the interval that contains its center.

Within each solid angle $\Delta\Omega_j^i$, $j=1,\ldots,J_i$, corresponding to $\Delta\theta_i$, the number of intercepted shots $N_{\text{itcp}}^{\Delta\Omega_j^i}$ is sampled over the distance with a step Δr (in our case, it equals 2 m as a consequence of a compromise between the precision of the results and the distribution of the detected points inside each interval). The sampling set is $\{r_k\}_{k=1,\ldots}$. $N_{\text{itcp}}^{\Delta\theta_i}(r_k,\Delta r)$ is given by

$$N_{\text{itcp}}^{\Delta\theta_i}(r_k,\Delta r) = \frac{1}{J_i}\sum_{j=1,\ldots,J_i}\frac{N_{\text{itcp}}^{\Delta\Omega_j^i}(r_k,\Delta r)}{\Delta\Omega_j^i} \tag{6}$$

where $N_{\text{itcp}}^{\Delta\Omega_j^i}(r_k,\Delta r)$ is the number of shots intercepted in solid angle $\Delta\Omega_j^i$ in the distance interval $[r_k, r_k+\Delta r]$.

The density can be approximated by

$$n_{\text{itcp}}^{\Delta\theta_i}(r_k) = \frac{N_{\text{itcp}}^{\Delta\theta_i}(r_k,\Delta r)}{\Delta r}. \tag{7}$$

The exponential decreasing function, $A\exp(-\alpha r)$, is fit using the samples $n_{\text{itcp}}^{\Delta\theta_i}(r_k)$, $k=1,2,\ldots$.

After $N_{\text{tot}}^{\Delta\theta_i}$ derivation, one has

$$N_{\text{tot}}^{\Delta\Omega_j^i} = \Delta\Omega_j^i \times N_{\text{tot}}^{\Delta\theta_i},\ \ j=1,\ldots,J_i. \tag{8}$$

For a given voxel v observed within a solid angle $\Delta\Omega_v$ belonging to the sphere solid angle $\Delta\Omega_j^i$, the total number of shots, N_{tot}^v, is given by

$$N_{\text{tot}}^v = \frac{\Delta\Omega_v}{\Delta\Omega_j^i}\times N_{\text{tot}}^{\Delta\Omega_j^i}. \tag{9}$$

2) Estimation of u_l Based on Voxel Average Path-Length: Traditional Technique: In the literature, transmittance calculation using TLS data in each voxel v observed with a solid angle, $\Delta\Omega_v$, is defined as the ratio between the number of shots leaving the voxel, N_{out}^v, to the total number of TLS shots entering to it, N_{tot}^v [18]

$$T(\Delta\Omega_v) = \frac{N_{\text{out}}^v}{N_{\text{tot}}^v} = 1 - \frac{N_{\text{itcp}}^v}{N_{\text{tot}}^v - N_{\text{befor}}^v} \tag{10}$$

where N_{itcpt}^v is the intercepted number of shots and practically it is the number of TLS points in each voxel and N_{befor}^v is the number of rays propagating within the solid angle $\Delta\Omega_v$ intercepted before reaching v. Based on (1), u_l could be derived as

$$\hat{u}_l = -\frac{\log T}{G_{\text{LAD}}(\theta_v)\overline{\Delta L}}. \tag{11}$$

Combining (10) and (11), the estimated density, $\hat{u}_l$, can be calculated as

$$\hat{u}_l = -\frac{\log\left(1-\frac{N_{\text{itcp}}^v}{N_{\text{tot}}^v - N_{\text{befor}}^v}\right)}{G_{\text{LAD}}(\theta_v)\overline{\Delta L}} \tag{12}$$

where θ_v is the average zenith angle within $\Delta\Omega_v$ and $\overline{\Delta L}$ is the mean path length of the rays that pass through the voxel. Here, u_l need to be calculated based on (12) for each voxel. To do it, the mean path-length, which is variable from a ray to another within the voxel is considered.

3) Estimation of u_l Based on Voxel Partitions Path-Length: Novel Technique: Averaging all the path passing through voxels (12) could bias the $\hat{u}_l$ values since in this case, all the rays are assumed traveling the same distance $\overline{\Delta L}$ over the voxel v, which is not the case as many rays are traveling long distance in the middle of the voxel whereas others are crossing the voxel in the border with only a small path. In the latter case, the probability to be intercepted is very low. This effect increases the transmittance and, therefore, decreases the values of the estimate u_l.

To overcome this problem, we propose to deal with the distribution of $u_l(L)$ as a function of the traveling distance, L, and

then average the result to derive the voxel density. Therefore, it is required to define the probability distribution function of distance f_L that allows us to inform us about the presence, and therefore, the importance of each possible distance within the voxel.

Moreover, the probability of vegetation hit is proportional to the distance, it means that shortest distances are less informative about the vegetation density as this probability is too low in this case. It becomes nonnegligible for longest paths. This means that when averaging, $u_l(L)$, over L to estimate the voxel density $\hat{u}_l$, it is necessary to give more importance to the longest distance. One can write

$$\hat{u}_l = \mathbb{E}[u_l(L)] = \int_L u_l(L).f_{u_l}(L).\mathrm{d}L \tag{13}$$

where $\mathbb{E}$ is the expectation operator and f_{u_l} is the distance importance function.

As a first approximation, it is possible to put $f_{u_l} = f_L$. However, to give more importance to the longest distance we assume that f_{u_l} is proportional to $L \times f_L$. Therefore, to ensure $\int f_{u_l} = 1$, one can write

$$f_{u_l}(L) = \frac{L f_L(L)}{\int_L u_l(L) f_{u_l}(L)\mathrm{d}L}. \tag{14}$$

In practical point of view, the distance distribution is divided up into N intervals. f_L is replaced by the weight set $\{\alpha_i\}_{i=1,\ldots,N}$. In this case

$$\int_L u_l(L) f_{u_l}(L)\mathrm{d}L = \sum_i L_i \alpha_i. \tag{15}$$

f_{u_l} is also discretized into the set $\{\alpha_i^{u_l}\}_{i=1,\ldots,N}$ such as

$$\alpha_i^{u_l} = \frac{L_i \alpha_i}{\sum L_j \alpha_j}. \tag{16}$$

$\hat{u_l}$ is estimated as follows:

$$\hat{u_l} = \sum_i u_l(L_i)\alpha_i^{u_l} = -\sum_i \frac{\log(T_i)}{L_i G_{\mathrm{LAD}}}\alpha_i^{u_l}. \tag{17}$$

Equations (12) and (17) corresponding to the estimation using the traditional and the new developed methods are different. They produce the same results when the path length L variation is too small. Otherwise, the difference is non-negligible mainly because the estimation is not linear as a function of L in particular for the log function. This effect is more pronounced when $T \ll 1$. This point will be stressed in our experimental results.

4) Joint Estimation of u_l and LAD: For each voxel, u_l cannot be calculated unless a default LAD distribution is presumed but the result could be incorrect otherwise LAD should be assessed, too. This work selects the second alternative, with u_l and LAD joint estimation. Remembering that LAD is defined through the LIDF $f(\theta_l)$, $\theta_l \in [0, \pi/2]$. As commonly suggested [30], f is sampled over $N_l = 15$ inclination intervals $\{\Delta\theta_{l,i}\}_{i=1,\ldots,N_l}$, centered on

$$\{\theta_{l,i}\}_{i=1,\ldots,N_l} = [5^\circ, 15^\circ, 25^\circ, 35^\circ, 45^\circ, 55^\circ, 64^\circ, 72^\circ, 77^\circ, 79^\circ, 81^\circ, 83^\circ, 85^\circ, 87^\circ, 89^\circ]. \tag{18}$$

It gives rise to the probabilities of inclination $\{P_l(\Delta\theta_{l,i})\}_{i=1,\ldots,N_l}$. Estimation of u_l and P_l for each voxel is an undercharacterized problem since one has only the transmittance expression to estimate 16 parameters. In our case, we assume that P_l is the same for the whole vegetation layer. This condition is not enough for our joint estimation problem to be solved and assumption over u_l must be given. u_l cannot be assumed the same for all the voxels as density can increase or decrease from a tree to another and within the same tree. Nevertheless, it is possible to assume that the average density $\bar{u}_l$ over the LiDAR observation azimuth angle, ϕ_o, is constant as a function of the zenith angle θ_o. This assumption is not too restrictive. It assumes that for each incident angle, the sensor observes all the possible density cases as it observes the bottom, the middle, and the top of the vegetation layer. In practical point of view, the zenith angle is divided up into N_o intervals, $\{\Delta\theta_{o,j}\}_{j=1,\ldots,N_o}$. In this case, it is possible to link $\bar{u}_l$ to u_l as follows:

$$\bar{u}_l(\Delta\theta_{o,j}) = \frac{\sum_{\theta_o^v \in \Delta\theta_{o,j}} u_l(r^v, \theta_o^v, \phi_o^v)}{\sharp\{v | v \in V, \theta_o^v \in \Delta\theta_{o,j}\}}. \tag{19}$$

V is the set of the voxels, $(r^v, \theta_o^v, \phi_o^v)$ are the spherical coordinates of the center of the voxel v belonging to the vegetation medium and for a given set E, $\sharp E$ is its cardinal. Note that in practical point of view, the sampling rate of the zenith angle was chosen equals 2°. It was possible to use such a precise rate since the number of voxels was important, so, averaging the foliage density over narrow intervals of the zenith angle was possible allowing, therefore, a high retrieval accuracy of the foliage density and LAD.

Given $\{P_l(\Delta\Omega_{l,i})\}_{i\in\{1,\ldots,N_l\}}$, it is possible to apply one of the techniques described previously (12) and (17) to derive u_l and $\bar{u}_l$.

In the following, our objective is to jointly derive the inclination probability and the voxel density sets $\{u_l(V)\}_{v\in V}$. The corresponding cost function should allow us to produce realistic probability and leaf area density. To ensure it, regularization assumptions are assumed. In particular, $\bar{u}_l$ variance should be minimized to reduce its variation from a zenith angle to another. Similarly, P_l variance should be reduced as well as its gradient. The latter ensures the correlation between close zenith angles and so the P_l smoothness. The global cost function c is, therefore, given by

$$c(\{P_l(\Delta\Omega_{l,i})\}_{i\in\{1,\ldots,N_l\}}) = \sigma^2(\bar{u}_l) + \alpha \times \sigma^2(P_l) + \beta \times \nabla(P_l) \tag{20}$$

where σ^2 and ∇ are the variance and gradient operators, respectively, and α and β two fixed parameters to balance the cost. They are put equal to 1 and 0.5, respectively.

According to (20), it is clear that we face a nonlinear problem where the solution space is not convex and an optimization process could converge toward local optima. To deal with the problem, the shuffled complex evolution (SCE-UA) [33], [34] global search method is adopted to our problem. This approach applies a parallel search within the variable space using a set of potential solutions. The capacity of such a kind of strategy

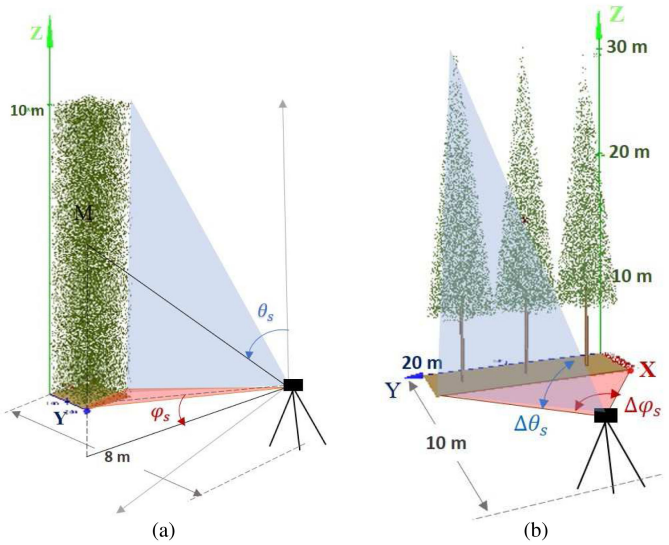

Fig. 5. TLS observes the two types of created simulated vegetation scenes, (a) homogeneous scene composed of randomly distributed leaves, (b) heterogeneous scene composed of three trees. In (a), vegetation layer size is 2 m × 2 m × 10 m. In (b), each tree is of a size 6 m × 6 m × 30 m. TLS zenith and azimuth angles are (θ_s, φ_s). Its field of views are $(\Delta\theta_s, \Delta\varphi_s)$.

for a successful exploration of all the space makes them less likely to be stuck in local optima; therefore, it belong to the global heuristics. It incorporates the best features of multiple local heuristics in competitions called complex and inspired from the simplex search method [35]. Its process is described succinctly as follows. Initially, a random set of potential solutions composed of a series of the parameters to be optimized is generated within the bounds given for each parameter. Next these potential solutions are sorted based on the value of the cost function and partitioned into several complexes. Each complex is then evolved independently according to the simplex algorithm. Then, the second generation is produced by combining all the solutions in each complex. The sorting step is after that repeated and complexes are shuffled. This process is repeated until the convergence is reached. In this study, initially, optimization targets are the set of probabilities $\{P_l^j\}_{j\in\{1,\ldots,N\}}$. $N = m \times p$, where m is the size of each complex (it equals $2 \times N_l + 1$ as suggested in [33] and [36]), and p is the number of partitioned complexes (here $p = 12$ was chosen based on experimental tests).

For a given j, each element of the vector P_l^j: $P_l^j(\Delta\Omega_{l,i})$ $(i = 1, \ldots, N_l)$ is sampled from the $[0, 1]$ space, checking that $\sum_{i=1}^{N_l} P_l^j(\Delta\Omega_{l,i}) = 1$. Then, the aforementioned SCE-UA method steps are carried out until convergence. More detailed description about the optimization algorithms are found in Appendices A and B.

V. Experimental Results

A. Simulated Data: Forward Model

Recalling that two types of simulated scenes are created in this work, as shown in Fig. 5. The first set of data is composed of homogeneous scenes considered for a feasibility study of our methods. The second set of data is heterogeneous scene composed of trees is created to be closer to actual forest 3-D representation. In the first set of scenes, as shown in Fig. 5(a), leaves were represented by disks randomly distributed in a parallelepiped of dimension (2 m × 2 m × 10 m). Scenes were simulated using two different u_l values (0.2 m^2 m^{-3} and 0.4 m^2 m^{-3}) and three different LADs (planophile, erectophile, and spherical).

The TLS sensor, located at the position $(X, Y, Z) = (8\text{ m}, 1\text{ m}, 1\text{ m})$, scans the scenes varying the zenith angle θ_s and the azimuth angle φ_s in the intervals $[34°, 98°]$ and $[-10°, 10°]$ with sampling steps equal to $0.42°$ and $0.01°$, respectively.

For the second set of scenes, two distinct shapes of tree crowns are created: 3-D conical trees of identical size, 30 m height and 3 m radius, were created inside an earth scene of dimension (20 m × 6 m), as shown in Fig. 5(b). u_l value is considered equal 0.7 m^2 m^{-3} and two LIDFs planophile and erectophile. Trees were positioned at $(X, Y) = \{(3\text{ m}, 3\text{ m}), (10\text{ m}, 3\text{ m}), (17\text{ m}, 3\text{ m})\}$ in the scene coordinate system, whereas the TLS sensor is located at $(X, Y, Z) = (10\text{ m}, 10\text{ m}, 1\text{ m})$. Besides, 3-D elliptical tree crowns of identical size, 30 m height and 5 m diameter, were set within an earth scene of dimension (20 m × 5 m). u_l value is considered equal 0.8 m^2 m^{-3} and spherical LIDF. Trees were positioned at $(X, Y) = \{(3\text{ m}, 2.5\text{ m}), (10\text{ m}, 2.5\text{ m}), (17\text{ m}, 2.5\text{ m})\}$ in the scene coordinate system, whereas the TLS sensor is located at $(X, Y, Z) = (10\text{ m}, 10\text{ m}, 1\text{ m})$.

For both tree shapes, the scan FOV was set to fit with the size of the tree crowns varying the zenith angle θ_s and the azimuth angle φ_s in the intervals $[30°, 110°]$ and $[20°, 160°]$, respectively, with the same sampling steps equal to $0.025°$.

The sampling resolution is higher than the one for the homogeneous case in order to generate high accuracy even through in border voxels.

In our study, the point cloud was voxelized to jointly estimate u_l and LAD at 0.25 m, 0.5 m, and 1 m voxel sizes (S_{vox}). In this way, the influences of voxel size on results accuracy were assessed by comparing the simulated data against the actual values.

The ray-tracing algorithm is used to simulate the scan of the created mock-ups with the TLS sensor. The virtual laser beams were generated based on the scanning geometry. Then, the interception of the laser beams and leaves within voxels is calculated. Fig. 6 presents the 3-D scanning results of the homogeneous and heterogeneous scenes.

For the homogeneous scene drawn in Fig. 6(a), u_l equals 0.4 m^2 m^{-3} and LAD is planophile whereas for the heterogeneous scene point cloud presented by Fig. 6(b) and (c) are (0.7 m^2 m^{-3}, Erectophile) and (0.8 m^2 m^{-3}, spherical), respectively.

The density of the point cloud in both representations could be influenced by many factors that can be categorized as factors related to geometric aspects such as the resolution and the geometry of the scan and factors related to the vegetation biophysical properties such as leaf density and orientation. Therefore, to fully understand the influence of the foliage property (u_l and LAD) variation on the interception and transmittance

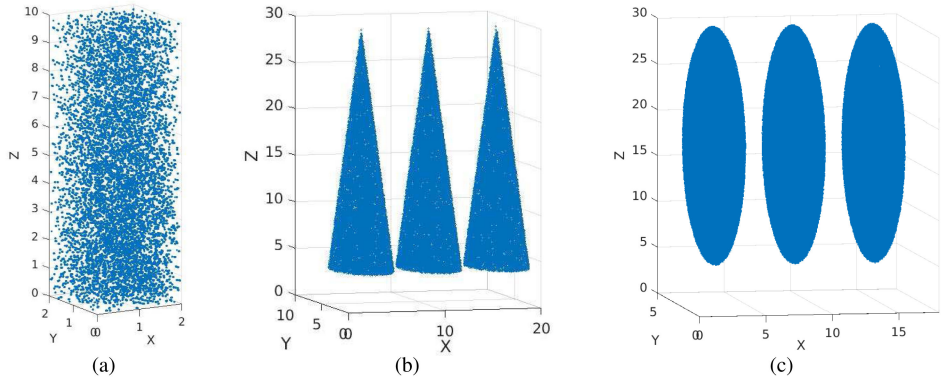

Fig. 6. Detected 3-D TLS point cloud of the observed scenes, (a) homogeneous scene point cloud with ($u_l = 0.4$ m^2 m^{-3}, planophile LIDF), (b) and (c) heterogeneous scenes point cloud with ($u_l = 0.7$ m^2 m^{-3}, ereclophile LIDF, conical crown) and ($u_l = 0.8$ m^2 m^{-3}, spherical LIDF, elliptical crown), respectively.

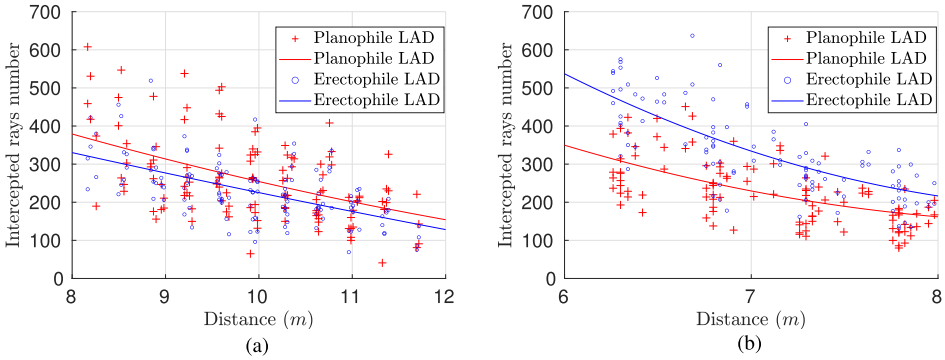

Fig. 7. Number of intercepted TLS rays per voxel as a function of the distance from the sensor to the corresponding voxel center for an erectophile and planophile LAD using $u_l = 0.4$ m^2 m^{-3}, (a) for small inclination angles of the sensor zenith view angle, $35° < \theta_s < 55°$, (b) for large sensor zenith angles, $70° < \theta_s < 90°$.

phenomena, a sensitivity analysis using the simulated point cloud of homogeneous scene is conducted in this study.

Recalling that, forest mock-ups were created using our own models as detailed earlier. The creation and modeling of laser beams inside the vegetation scene was established, thanks to our developed ray tracing technique.

1) Effect of LAD Variation on Point Cloud Detection: Fig. 7 demonstrates the effect of LAD on the number of the intercepted TLS shots per each voxel as a function of distance from TLS sensor to voxel centers and compares small and large sensor zenith angles.

The red and blue curves indicate the fit of the detected rays for planophile and erectophile LAD, respectively.

For all simulations, the farther the distance from the sensor is the fewer is the number of detected points. This is due to the occlusion effect where close objects block the viewing direction. In Fig. 7(a), where the sensor zenith angle is small, despite the fixed value of $u_l = 0.4$ m^2 m^{-3}, a rise is observed in the number of intercepted points using planophile LAD. Actually, this is explained by two factors: the planophile LAD, i.e., horizontally oriented leaves and the relatively small inclination of the sensor viewing angle; θ_s ($35° < \theta_s < 55°$). Indeed, horizontal leaves (planophile) will have a considerably larger projected area on the laser sensor than the vertical ones (erectophile). Conversely, in Fig. 7(b), for large inclination of θ_s, where the sensor almost horizontally observes the scene, a highest number of intercepted points is observed in the erectophile case. This is expected since leaves are tending to the vertical unlike planophile LAD. Therefore, the probability to detect leaves is the highest for erectophile case.

Furthermore, the disparity between the two curves is variable as a function of distance. In general, the difference between the two distributions decreases since for the highest curve, the number of rays decreases rapidly and so the intercepted ray number. For instance, in Fig. 7(b), for erectophile LAD, the number of intercepted shots is decreased over a distance of 2.5 m by 70%, however, for planophile LAD, it decrease by 50% over the same distance. Therefore, we can conclude that the greater the possibility of interception for close ranges, the less likely it is to detect objects at further distances and vice versa.

2) Effect of u_l Variation on Point Cloud Detection: Fig. 8 shows the effect of u_l on the detected point cloud. The obtained curves present the fit of the number of the detected points within each voxel as a function of distance from the TLS position to voxels center for planophile and erectophile LAD. The red and blue curves correspond to u_l values equal 0.2 m^2 m^{-3} and 0.4 m^2 m^{-3}, respectively. The number of detected points decreases in all cases due to the occlusion effect as it is previously explained.

The blue curve is elevated compared to the red one in all the different situations. Here, we can notice that the foliage density is a highly influencing parameter. Indeed, the probability

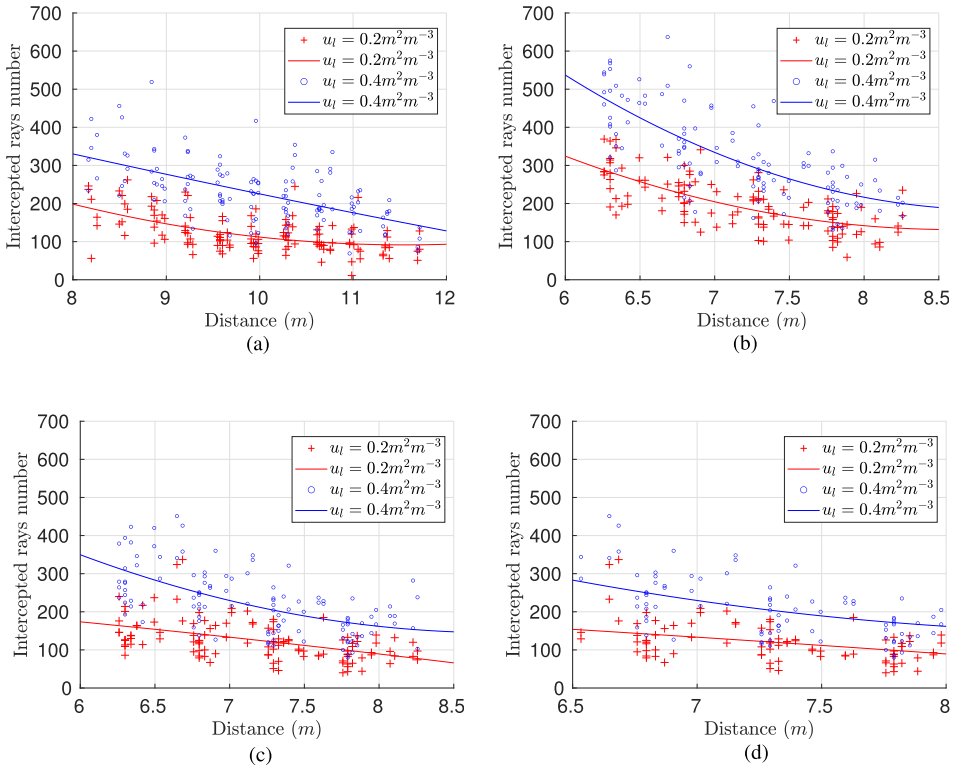

Fig. 8. Number of intercepted TLS rays per voxel as a function of the distance from the sensor to the corresponding voxel center for different LAD using $u_l = \{0.2\ \mathrm{m}^2\ \mathrm{m}^{-3}, 0.4\ \mathrm{m}^2\ \mathrm{m}^{-3}\}$, (a) and (b) erectophile LAD for small and large sensor zenith angles, respectively, (c) and (d) planophile LAD for small and large sensor zenith angles, respectively. (a) Erectophile LAD, $35° < \theta_s < 55°$. (b) Erectophile LAD, $70° < \theta_s < 90°$. (c) Planophile LAD, $35° < \theta_s < 55°$. (d) Planophile LAD, $70° < \theta_s < 90°$.

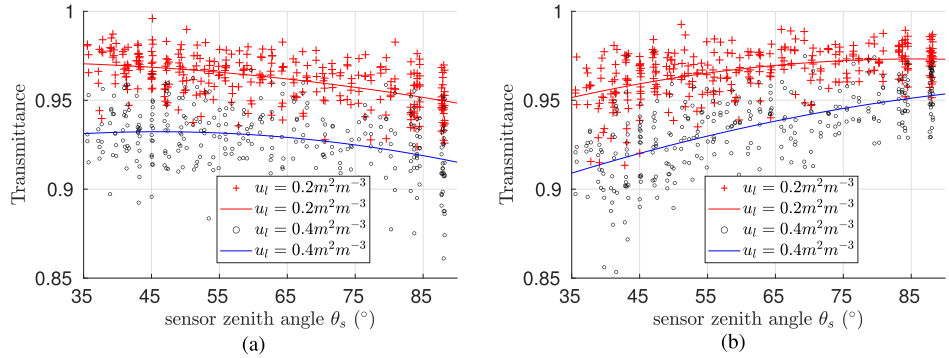

Fig. 9. Effect of u_l and LAD on transmittance values, (a) u_l variation for erectophile LAD, (b) u_l variation for planophile LAD. (a) Erectophile LAD. (b) Planophile LAD.

of interception is highly correlated to the leaf density. Moreover, the distance between the curves decreases as a function of depth as for the highest u_l value (blue) the number of rays and so the number of interceptions decreases too fast.

In terms of curves convergence, we see that the case erectophile, large zenith angle, and planophile, large zenith angle, provide the highest and the lowest rate, respectively. In fact, the former case correspond to the maximum interception rates and the decrease of the blue curve is, therefore, the fastest. Whereas in the last case, the interception rate is too low compared to the number of rays and the difference between the two curves is slowly varying.

3) Effect of LAD and u_l Variation on Transmittance Calculation: Fig. 9 shows the effect of the variation of the foliage density and LAD on transmittance for viewing angle varying from 30° to 90°. The red and blue curves present the fits for transmittance values calculated within each voxel as a function of the sensor zenith angle θ_s using $u_l = 0.2\ \mathrm{m}^2\ \mathrm{m}^{-3}$ and $u_l = 0.4\ \mathrm{m}^2\ \mathrm{m}^{-3}$, respectively.

For both LIDFs, the transmittance measured using the highest value of u_l is lower given the lower chance for TLS rays to pass through foliage without interception. Therefore, transmittance calculation is highly dependent on foliage density.

TABLE III
PERFORMANCES OF SIMULATION RESULTS OF HOMOGENEOUS SCENES, BIAS_{u_l} IS THE ABSOLUTE AVERAGE ERROR BETWEEN THE ACTUAL AND ESTIMATED u_l, RMSE_{u_l} IS THE ROOT MEAN SQUARE ERROR BETWEEN ACTUAL AND ESTIMATED u_l AND $\text{RMSE}_{\text{LIDF}}$ IS THE ROOT MEAN SQUARE ERROR OF LIDF

Performances / $(u_l, LIDF)$	1^{st} method			2^{nd} method		
	$Bias_{u_l}$	$RMSE_{u_l}$	$RMSE_{LIDF}$	$Bias_{u_l}$	$RMSE_{u_l}$	$RMSE_{LIDF}$
($0.2m^2m^{-3}$, planophile)	0.0024	0.0208	0.0338	0.0011	0.0209	0.0334
($0.4m^2m^{-3}$, planophile)	0.0099	0.0452	0.0396	0.0062	0.0450	0.0375
($0.2m^2m^{-3}$, erectophile)	0.0034	0.0192	0.0129	0.0033	0.0192	0.0188
($0.4m^2m^{-3}$, erectophile)	0.0079	0.0331	0.0229	0.0043	0.0319	0.0239
($0.2m^2m^{-3}$, spherical)	0.0028	0.0396	0.0156	0.0017	0.0250	0.0150
($0.4m^2m^{-3}$, spherical)	0.0031	0.0781	0.0096	0.0052	0.0356	0.0191
($1.5m^2m^{-3}$, erectophile)	0.0576	0.1821	0.0367	0.0283	0.1468	0.0369

A major shift in the form of curves is observed when passing from an LIDF to another. Multiple factors are connected to these modifications. For instance, in Fig. 9(a), the decrease in transmittance values as a function of θ_s is explained as follows. The probability of detecting vertically oriented leaves is reduced by decreasing the sensor zenith angle. Therefore, more escaped rays without interception and consequently higher transmittance values are observed in small inclination case. Conversely, important sensor zenith angles increases the probability of blocking and lower transmittance values are observed as a result. For the planophile LAD case, the reverse is true; low interception rate and so high transmittance occur for large sensor inclination explaining, therefore, the increasing shape of the curves in Fig. 9(b).

As a conclusion of this section, we can say that transmittance as well as its variation as a function of the incidence angle and the depth are highly depending on the leaf density and angular distribution. The sensitivity of the transmittance to these parameters makes their retrieval possible. The density of TLS rays is too high, which makes it possible to reach almost all voxel within the studied scene. Therefore, transmittance calculation and foliage properties estimation are possible for the majority of voxels. Nevertheless, it is important to mention that for fully occluded voxels, the estimation is not practical.

B. Simulated Data: Inverse Model

1) Homogeneous Data: The joint retrieval of u_l and LAD is carried out using both traditional and novel techniques in this work, hence, for the called first and second method, respectively. The shown results are obtained using a voxel size $S_{\text{vox}} = 0.5$ m. Afterward, a sensitivity study of voxel size on estimation results accuracy will be conducted for homogeneous and heterogeneous scene types.

Fig. 10 displays the homogeneous data estimation results of u_l ($u_l = 0.2$ m^2 m^{-3}, 0.4 m^2 m^{-3}) and the associated LAD (planophile, erectophile, and spherical).

Comparisons are given in terms of bias and root-mean-square error (RMSE) between the estimated and actual u_l values as well as the RMSE for LIDF assessment.

Results show agreement between estimated and actual u_l and LAD values using both resolution techniques. Table III presents the measured performances. Concerning LIDF retrieval, results for erectophile and spherical LAD are more accurate than plonophile case, e.g., using the novel technique for $u_l = 0.2$ m^2 m^{-3}, the $\text{RMSE}_{\text{LIDF}} = 0.0188$ for erctophile LAD and $\text{RMSE}_{\text{LIDF}} = 0.0150$ for spherical LAD compared to $\text{RMSE}_{\text{LIDF}} = 0.0334$ for planophile LAD.

The decrease of the performances in the latter case can be explained by the fact that the sensor is in front of the vegetation layer, it observes mainly with large inclination angles and in these cases horizontal leaves cross section is too small, and therefore, they are hardly detected. Therefore, as the planophile LIDF contains the highest percentage of horizontal leaves, the retrieval performances are the lowest. The performances decrease also with the increase of the leaf density. This is due to the increase of the number of leaves per voxels and the probability of mutual shadowing between leaves increasing, therefore, the estimation uncertainty.

For leaf density estimation results, the results of the retrieval using both techniques show that $\bar{u}_l$ estimates are almost a constant function of the sensor zenith angle for the two actual u_l values (0.2 m^2 m^{-3} and 0.4 m^2 m^{-3}) and for the different used LIDFs.

Comparing the estimated curves of $\bar{u}_l$, the bias and RMSE between actual and estimated u_l in Table III using all techniques, we note that the results are almost similar with a bias that does not exceed 1% and low values of RMSE_{u_l}.

The proximity of u_l estimation result can be mathematically explained as follows.

Recalling that both techniques are based on the Lambert law (1). So, when $u_l \ll 1$ m^2 m^{-3} and $\overline{\Delta L} \ll 1$, in our case $u_l = 0.2$ m^2 m^{-3}, 0.4 m^2 m^{-3}, and voxel size equal 0.5 m, T becomes close to 1. Therefore, it is possible to write(1) as

$$T = \exp(-G(\theta).u_l.\overline{\Delta}L(\theta)) \approx 1 - G(\theta).u_l.\overline{\Delta}L(\theta). \quad (21)$$

In this case, u_l estimation becomes almost a linear problem and u_l value estimated by the two techniques (12) and (17) produce close results. To emphasize the nonlinearity effect of dense voxels pointed out at the end of Section IV-B3, another simulation is created using erectophile LAD, $u_l = 1.5$ m$^2/m^3$ and estimation voxels of size (1 m × 1 m × 1 m). Fig. 11 shows the results of the joint estimation using the two adopted techniques and last row of Table III presents the quantitative indexes. Fig. 11(a) presents u_l estimation results. Here, it is clear that both estimated $\overline{u}_l$ curves are almost constant as functions of the sensor zenith angle, but using traditional technique $\overline{u}_l$ is underestimated with biais $= 0.0576$, whereas it equals 0.0283

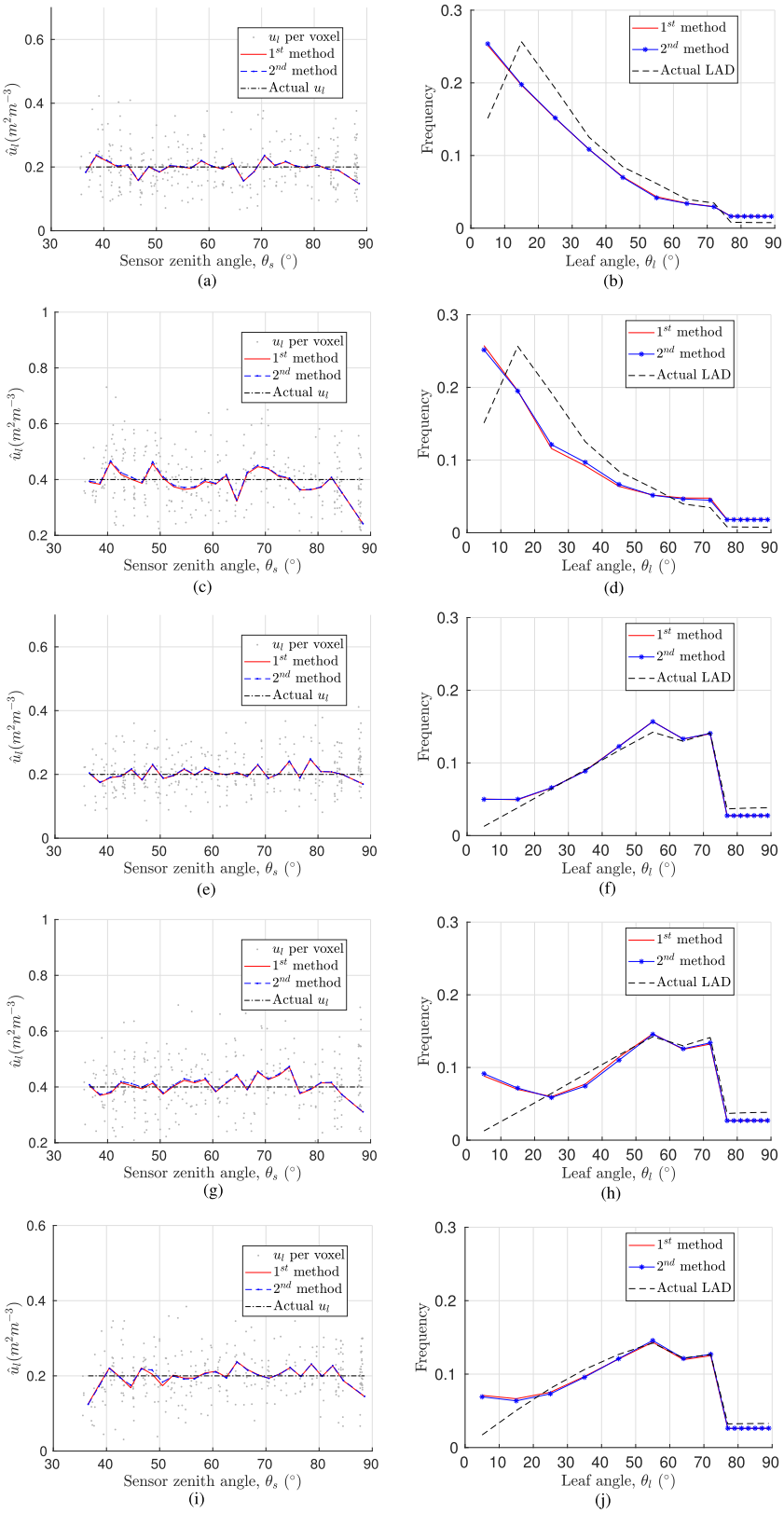

Fig. 10. Estimation of u_l and the corresponding LAD of homogeneous simulated data. (a), (c), (e), (g), (i), and (k) point cloud corresponds to u_l voxel estimation and curves correspond to the averaged $\overline{u}_l$ over 2° intervals. Rows u_l and LIDF properties are (0.2 m^2 m^{-3}, planophile), (0.4 m^2 m^{-3}, planophile), (0.2 m^2 m^{-3}, erectophile), (0.4 m^2 m^{-3}, erectophile), (0.2 m^2 m^{-3}, spherical), and (0.4 m^2 m^{-3}, spherical), respectively. (a) u_l estimation. (b) LAD estimation. (c) u_l estimation. (d) LAD estimation. (e) u_l estimation. (f) LAD estimation. (g) u_l estimation. (h) LAD estimation. (i) u_l estimation. (j) LAD estimation.

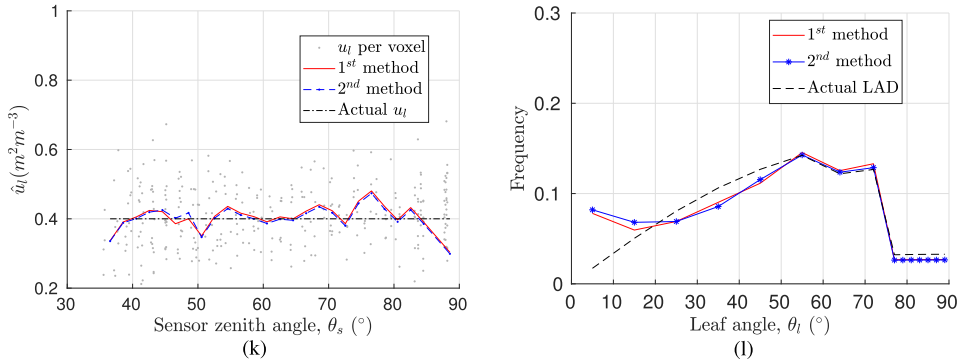

Fig. 10. (Continued.) (k) u_l estimation. (l) LAD estimation.

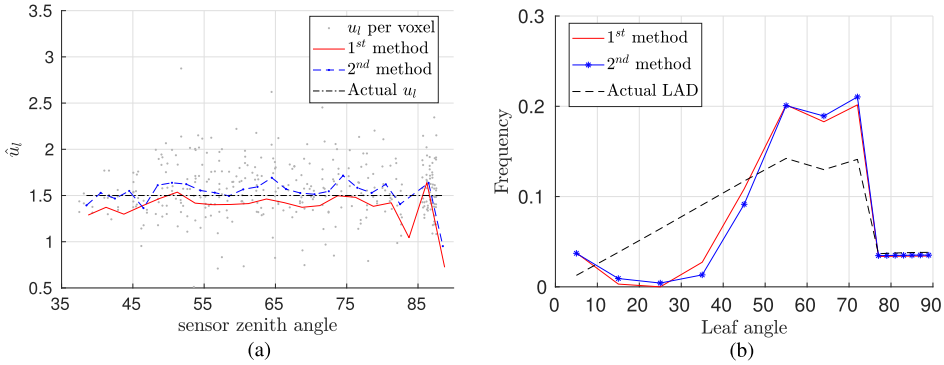

Fig. 11. Estimation of u_l and the corresponding LAD of homogeneous simulated data, (a) u_l estimation, (b) LAD estimation. LAD is erectophile, $u_l = 1.5$ m^2 m^{-3}, voxel size $= 1$ m $\times$ 1 m $\times$ 1 m.

TABLE IV
PERFORMANCES OF SIMULATION RESULTS OF HOMOGENEOUS SCENES USING A REDUCED NUMBER OF TOTAL TLS RAYS (SEE TABLE III FOR EXHAUSTIVE NOTATION EXPLANATION)

Performances / $(u_l, LIDF)$	1^{st} method			2^{nd} method		
	$Bias_{u_l}$	$RMSE_{u_l}$	$RMSE_{LIDF}$	$Bias_{u_l}$	$RMSE_{u_l}$	$RMSE_{LIDF}$
($0.4m^2m^{-3}$, erectophile)	0.0707	0.1198	0.0361	0.0247	0.0884	0.0175
($0.4m^2m^{-3}$, planophile)	0.0545	0.1227	0.0465	0.0437	0.0879	0.0209

for the novel technique. This result prove that the traditional technique performance decreases with the leaf area per voxel.

There are several variables that influence the accuracy of u_l and LAD retrieval, while their distributions are the key factors, the resolution of the TLS point cloud and voxel size affect the results.

a) The influence of TLS point cloud angular resolution on the accuracy of the retrieved properties: To quantify this effect, Fig. 12 draws the estimated results using a reduced number of total TLS rays to 250 per voxel rather than 4000 rays/voxel. Table IV illustrates the corresponding quantitative measurements.

With all the simulations, the obtained results are degraded compared to those shown with 4000 rays/voxel ($S_{\text{vox}} = 0.5$ m) (see Table III). Moreover, comparing results in Fig. 12(a) and (c) shows that the estimated $\overline{u}_l$ curves for the novel technique present more accurate retrieval than the traditional one in both LAD cases. The same observation is valid for LAD estimation and justified by the measured performances presented in Table IV. In conclusion, the more accurate and denser the sampled data are, the more precise results are obtained.

b) The influence of voxel size on the accuracy of retrieved properties for homogeneous data: To see how voxel size affects u_l and LAD retrieval accuracy, all simulated cases were performed with three different voxel sizes ($S_{\text{vox}} = 0.25$ m, 0.5 m, and 1 m). Tables V and VI summarize the measured results with a variation in voxel size, utilizing both traditional and novel strategies for u_l and LAD retrieval, respectively.

With all voxel sizes, the novel technique outperforms the traditional one in respect of u_l retrieval results. When comparing the estimation accuracy of the different voxel sizes for homogeneous data, it is clear that increasing the voxel size improves the estimation accuracy in general. For instance, RMSE$_{u_l}$ is reduced from 0.0644 using $S_{\text{vox}} = 0.25$ m to 0.0165 using $S_{\text{vox}} = 1$ m

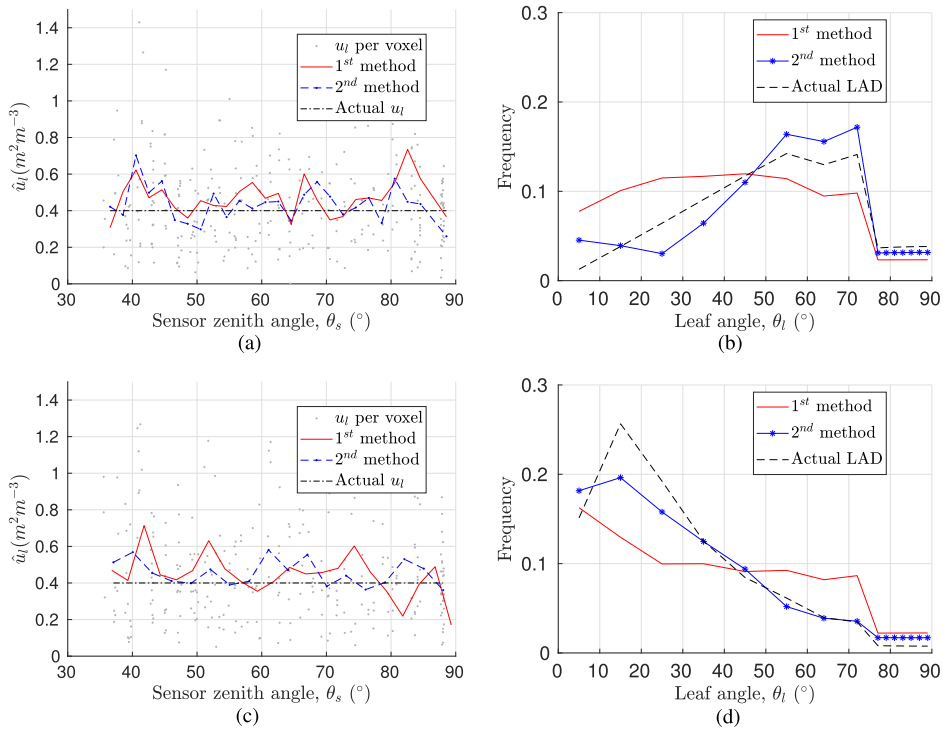

Fig. 12. Estimation of u_l and the corresponding LAD of homogeneous simulated data using reduced sampling rate, (a) u_l estimation, (b) LAD estimation. LAD are erectophile and planophile, $u_l = 0.4$ m^2 m^{-3}.

TABLE V
PERFORMANCES OF u_l ESTIMATES OF HOMOGENEOUS SCENES USING DIFFERENT VOXEL SIZES S_{VOX} (0.25 M, 0.5 M, 1 M), (SEE TABLE III FOR EXHAUSTIVE NOTATION EXPLANATION)

	$S_{vox} = 0.25m$				$S_{vox} = 0.5m$				$S_{vox} = 1m$			
	1^{st} method		2^{nd} method		1^{st} method		2^{nd} method		1^{st} method		2^{nd} method	
Performances / $(u_l, LIDF)$	$Bias_{u_l}$	$RMSE_{u_l}$	$Bias_{u_l}$	$RMSE_{u_l}$	$Bias_{u_l}$	$RMSE_{u_l}$	$Bias_{u_l}$	$RMSE_{u_l}$	$Bias_{u_l}$	$RMSE_{u_l}$	$Bias_{u_l}$	$RMSE_{u_l}$
($0.2m^2m^{-3}$, planophile)	0.0683	0.0729	0.0593	0.0644	0.0024	0.0208	0.0011	0.0209	0.0136	0.0159	0.0125	0.0165
($0.2m^2m^{-3}$, erectophile)	0.0494	0.0563	0.3630	0.0508	0.0034	0.0192	0.0033	0.0192	0.0086	0.0109	0.0039	0.0207
($0.2m^2m^{-3}$, spherical)	0.0480	0.0521	0.0327	0.0483	0.0028	0.0396	0.0017	0.0250	0.0007	0.0239	0.0005	0.0245
($0.4m^2m^{-3}$, planophile)	0.0370	0.0484	0.0476	0.0683	0.0099	0.0452	0.0062	0.0450	0.0122	0.0301	0.0083	0.0378
($0.4m^2m^{-3}$, erectophile)	0.0390	0.0573	0.0133	0.0586	0.0076	0.0331	0.0043	0.0319	0.0002	0.0264	0.0024	0.0235
($0.4m^2m^{-3}$, spherical)	0.0002	0.0186	0.0031	0.0211	0.0031	0.0781	0.0052	0.0356	0.0002	0.0186	0.0010	0.0201

TABLE VI
PERFORMANCES OF LAD ESTIMATES OF HOMOGENEOUS SCENES USING DIFFERENT VOXEL SIZES S_{VOX} (S_{VOX}= 0.25 M, 0.5 M, 1 M), (SEE TABLE III FOR EXHAUSTIVE NOTATION EXPLANATION)

	$S_{vox} = 0.25m$		$S_{vox} = 0.5m$		$S_{vox} = 1m$	
$RMSE_{LIDF}$ / $(u_l, LIDF)$	1^{st} method	2^{nd} method	1^{st} method	2^{nd} method	1^{st} method	2^{nd} method
($0.2m^2m^{-3}$, planophile)	0.0130	0.0352	0.0338	0.0334	0.0342	0.0353
($0.2m^2m^{-3}$, erectophile)	0.0464	0.0463	0.0129	0.0188	0.0444	0.0462
($0.2m^2m^{-3}$, spherical)	0.0142	0.0202	0.0156	0.0150	0.0217	0.0235
($0.4m^2m^{-3}$, planophile)	0.0201	0.0311	0.0396	0.0375	0.0395	0.0300
($0.4m^2m^{-3}$, erectophile)	0.0229	0.0234	0.0229	0.0239	0.0252	0.0169
($0.4m^2m^{-3}$, spherical)	0.0151	0.0178	0.0096	0.0191	0.0151	0.0215

TABLE VII
PERFORMANCES OF SIMULATION RESULTS OF HETEROGENEOUS SCENES (SEE TABLE III FOR EXHAUSTIVE NOTATION EXPLANATION)

	1^{st} method			2^{nd} method		
Performances / $(u_l, LIDF)$	$Bias_{u_l}$	$RMSE_{u_l}$	$RMSE_{LIDF}$	$Bias_{u_l}$	$RMSE_{u_l}$	$RMSE_{LIDF}$
($0.7m^2m^{-3}$, planophile)	0.0679	0.0902	0.0323	0.0454	0.0793	0.0134
($0.7m^2m^{-3}$, erectophile)	0.0134	0.0328	0.0143	0.0118	0.0298	0.0178
($0.8m^2m^{-3}$, spherical)	0.0106	0.0622	0.0128	0.0013	0.0501	0.0113

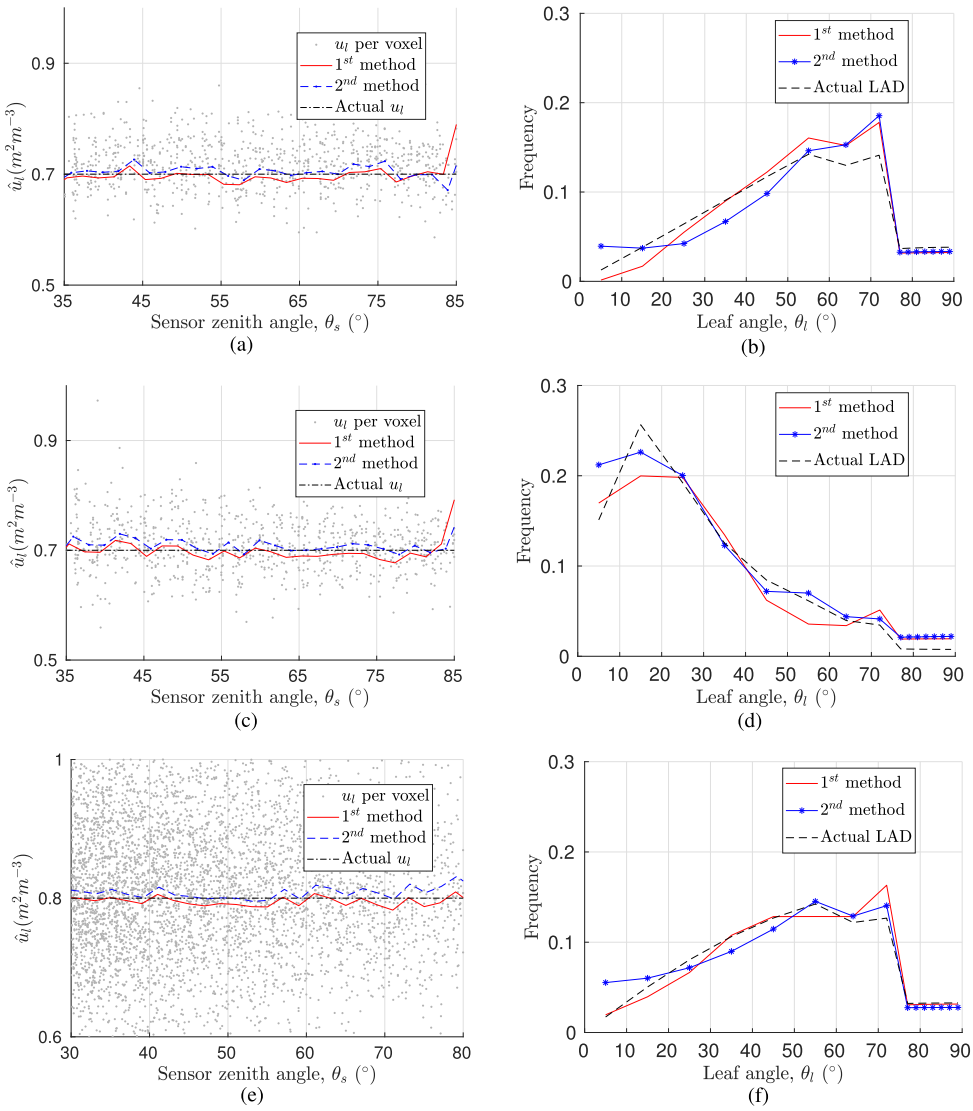

Fig. 13. Estimation of u_l and LAD of heterogeneous simulated TLS data using conical trees with erectophile and planophile LAD in first and second rows and elliptical trees with spherical LAD in third row, respectively. Red and blue curves correspond to the averaged u_l over 2° intervals. Point cloud corresponds to u_l voxel estimation. Actual $u_l = 0.7$ m^2 m^{-3} for conical trees and $u_l = 0.8$ m^2 m^{-3} for elliptical trees, $S_{\text{vox}} = 0.5$ m.

for the (0.2 m^2 m^{-3}, planophile, second method) simulation case.

This may be explained by the fact that when voxel size gets smaller, fewer pulses can enter the voxel, causing the statistics on transmission to be less reliable, and conversely, larger voxels are more capable of containing returns and are sampled by a higher number of TLS shots, resulting in more reliable u_l estimations in a homogeneous vegetation scene.

In respect of LAD retrieval, the results employing the novel technique are also better in all the simulation cases. Voxel size variation, in contrary, has no significant impact on measured performance. This is can be explained by the fact that LAD is estimated by averaging u_l over zenith angle intervals. This averaging operator reduces the uncertainty. Therefore, LAD retrieval is unaffected by voxel size change, which might be regarded as a strength of our approach.In sum, the quality of the results proves the validity of the joint estimation assumption in homogeneous case mainly for small leaf area per voxel (i.e., $u_l.\Delta L \ll 1$), a correct sampling rate and a suitable voxel size.

2) Heterogeneous Data: Fig. 13 shows the foliage parameters estimation results of heterogeneous scenes. Results show that similar results can be obtained using different resolution techniques. Nevertheless, compared to actual u_l values, the traditional technique estimates provide an underestimated $\overline{u}_l$ curves.

It is worth noting that the disparity of the point cloud of estimated u_l per voxel in the elliptical crown shape simulation, as shown in Fig. 13(e), is greater than in the conical situations, which is explained by the higher number of voxels within the crown.

The performances indicators of both strategies are presented in Table VII. The comparison between RMSE$_{u_l}$ shows a decline

TABLE VIII
PERFORMANCES OF u_l ESTIMATES OF HETEROGENEOUS SCENES USING DIFFERENT VOXEL SIZES S_{VOX} (S_{VOX}= 0.25 M, 0.5 M, 1 M), (SEE TABLE III FOR EXHAUSTIVE NOTATION EXPLANATION)

	$S_{vox} = 0.25m$				$S_{vox} = 0.5m$				$S_{vox} = 1m$			
	1^{st} method		2^{nd} method		1^{st} method		2^{nd} method		1^{st} method		2^{nd} method	
Performances / $(u_l, LIDF)$	$Bias_{u_l}$	$RMSE_{u_l}$	$Bias_{u_l}$	$RMSE_{u_l}$	$Bias_{u_l}$	$RMSE_{u_l}$	$Bias_{u_l}$	$RMSE_{u_l}$	$Bias_{u_l}$	$RMSE_{u_l}$	$Bias_{u_l}$	$RMSE_{u_l}$
($0.7m^2m^{-3}$, planophile)	0.0832	0.1035	0.0805	0.1002	0.0679	0.0902	0.0454	0.0793	0.0702	0.0942	0.0632	0.0954
($0.7m^2m^{-3}$, erectophile)	0.0785	0.0801	0.0755	0.0774	0.0134	0.0328	0.0118	0.0298	0.0314	0.0519	0.0283	0.0417
($0.8m^2m^{-3}$, spherical)	0.0425	0.0984	0.0105	0.0981	0.0109	0.0622	0.0013	0.0501	0.0325	0.0821	0.0196	0.1075

TABLE IX
PERFORMANCES OF LAD ESTIMATES OF HETEROGENEOUS SCENES USING DIFFERENT VOXEL SIZES S_{VOX} (S_{VOX}= 0.25 M, 0.5 M, 1 M), (SEE TABLE III FOR EXHAUSTIVE NOTATION EXPLANATION)

	$S_{vox} = 0.25m$		$S_{vox} = 0.5m$		$S_{vox} = 1m$	
$RMSE_{LIDF}$ / $(u_l, LIDF)$	1^{st} method	2^{nd} method	1^{st} method	2^{nd} method	1^{st} method	2^{nd} method
($0.7m^2m^{-3}$, planophile)	0.0341	0.0313	0.0323	0.0134	0.0331	0.0224
($0.7m^2m^{-3}$, erectophile)	0.0238	0.0204	0.0143	0.0178	0.0189	0.0187
($0.8m^2m^{-3}$, spherical)	0.0201	0.0158	0.0128	0.0113	0.0139	0.0139

in performances in the planophile case which corresponds to the high percentage of horizontal leaves which are hardly detected by a sensor in front of the trees. In addition, the comparison of the accuracy of the two techniques in terms of u_l retrieval shows an improvement using the novel technique.

The estimated value of LAD also indicates an agreement with the actual LIDFs. In specific, the measured $\text{RMSE}_{\text{LIDF}}$ is very low for erectophile and spherical LADs as it is easier to detect highly inclined leaves in our geometrical configuration.

The influence of voxel size on the accuracy of retrieved properties for heterogeneous data: In contrast to the homogeneous case, the voxel size here may have a considerable effect on the results due to the variability and heterogeneity of the vegetation. Tables VIII and IX summarize the measured performances for u_l and LAD assessment, respectively, by varying the voxel size using both retrieval techniques.

For all the voxel sizes, good agreement was exhibited between the estimated and the actual u_l with variation in accuracy. It can be seen from Table VIII that u_l performances are lower for small voxel size ($S_{\text{vox}} = 0.25$ m), reach better accuracy for $S_{\text{vox}} = 0.5$ m, and then decrease again as voxel size increases.

The decrease in u_l estimates at smaller voxel can be explained by the reduced number of pulses entering the voxel, causing less reliable statistics. Besides, it is important to notice in this case that the dataset become too large and took too much processing time.

The decrease in LAI estimates precision at larger voxel is because voxels of 1 m size contain large empty spaces belonging outside the crown. As voxel size increases, so does the probability of heterogeneous volume that violates the assumption of homogeneous distribution within the voxel. Therefore, u_l derivation accuracy is reduced.

The best results are obtained using $S_{\text{vox}} = 0.5$ m, which does a compromise between the number of TLS shots entering the voxels and the size and distributions of foliage within them. As in the homogeneous case, the derived LAD values were robust against voxel size variation, which only slightly decreased with changing voxel size with best result at $S_{\text{vox}} = 0.5$ m.

In this study, our created simulations mimic the reality of forest heterogeneity by relying on a diversification of input parameters such as tree shapes, foliage density values, and LIDF types, for that reason, the optimal voxel size for simulated data is considered in actual data processing.

C. Actual Data

1) Number of Total TLS Rays Estimation in Solid Angle: Fig. 14 is a representation of TLS data of the three forest stands considered in this study. The green point cloud corresponds to tree crowns and brown points corresponds to the detected tree trunks. The TLS point cloud was divided up into $(0.5\text{ m} \times 0.5\text{ m} \times 0.5\text{ m})$ voxels.

In this study, tree trunks were detected using the method suggested in [31], which consists of a specific 3-D clustering procedure. In this approach, tree stem cross-sections are approximated by a circle shape fitting method, which requires a segmentation of the point cloud. Trunks are finally defined as stacks of horizontal circles. Moreover, voxels containing trunk points were omitted from the calculation of u_l and LAD to ensure a reasonable estimation of the inspected properties.

Nevertheless, the latter are only removed from the estimation process of u_l and LAD but they are taken into consideration in the approximation of the number of total TLS rays per voxel and transmittance calculation. Recalling that different steps were taken into account to determine the number of total TLS shots per voxel, as described in Section IV-B1, based on the fact that the number of shots per solid angle, and thus, the number of intercepted shots decreased exponentially as a function of the distance to the sensor due to the occlusion effect. Fig. 15 draws the average number of total TLS shots within some zenith angle intervals of width 10° as a function of the distance to the TLS location. In addition to the average number of TLS point cloud, Fig. 15 plots the curves corresponding to the best points fitting

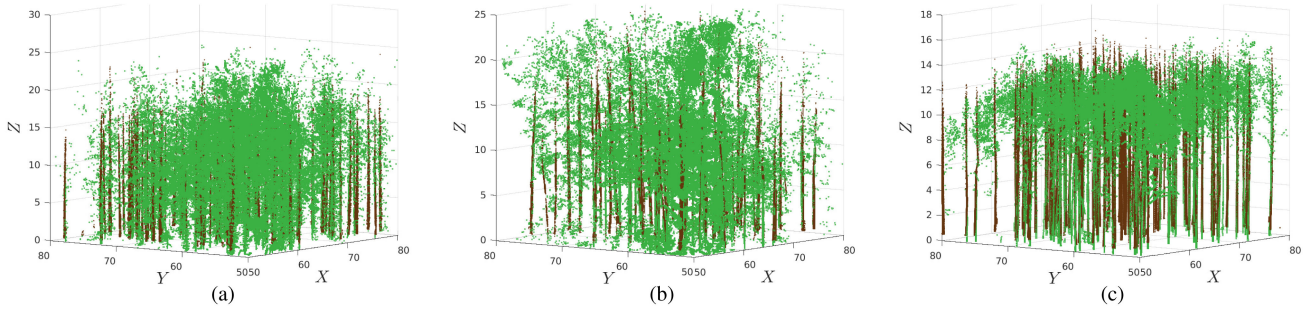

Fig. 14. Representation of the actual TLS data of Birch, Spruce, and Pine stands. Brown points correspond to tree trunks and green point cloud correspond to tree crowns.

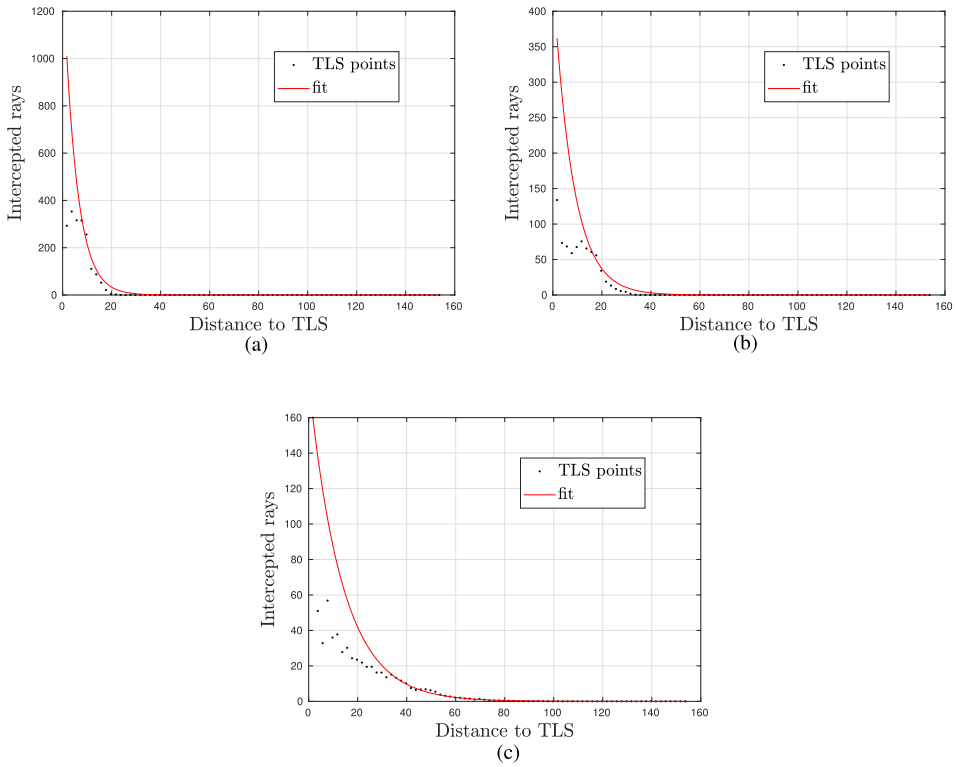

Fig. 15. Average number of TLS point cloud over solid angles in a given zenith angle interval as a function of the distance TLS-voxel. (a) for small inclination viewing angle $10^\circ < \theta < 20^\circ$, (b) for medium inclination $40^\circ < \theta < 50^\circ$, and (c) for large inclination $80^\circ < \theta < 90^\circ$.

according to a decreasing exponential function assuming an infinite size of the scene (4).

For instance, in Fig. 15(a), zenith angle of small inclination where $10^\circ < \theta < 20^\circ$ is considered, it is noted that the observed points are restricted to close distances to TLS (20 m), which is clearly the result of interception of rays with tree tops as the sensor is oriented to the sky in this configuration. In contrast, there are no detected points for extended ranges owing that the TLS shots have escaped the canopy.

In the case of $40^\circ < \theta < 50^\circ$, as shown in Fig. 15(b), many tree crowns are observed, more points are detected as a function of distance compared to the small inclination case, so fewer escaped shots.

For $80^\circ < \theta < 90^\circ$, tree trunks are well observed here, nearly all TLS shots are intercepted. The fitting is too accurate in this case mainly far from the sensor as the vegetation sampling becomes more random and statistically more representative. Contrariwise, close to the sensor only a fewer number of trees is observed increasing, and therefore fitting uncertainty.

2) Inversion Results: Fig. 16 shows the estimated u_l and the corresponding LAD for Pine, Spruce, and Birch stands using both techniques of our developed approach. To facilitate the result interpretation the closest spherical distribution to the novel technique is shown for each stand.

The extent of the point cloud in u_l retrieval plots, shows that the estimated values per voxel varies greatly due to the heterogeneity of the forest structure, and hence, the variability of the leaf density in each voxel and the estimated noise. Averaging u_l over zenith angle sensor significantly decreases noise as seen

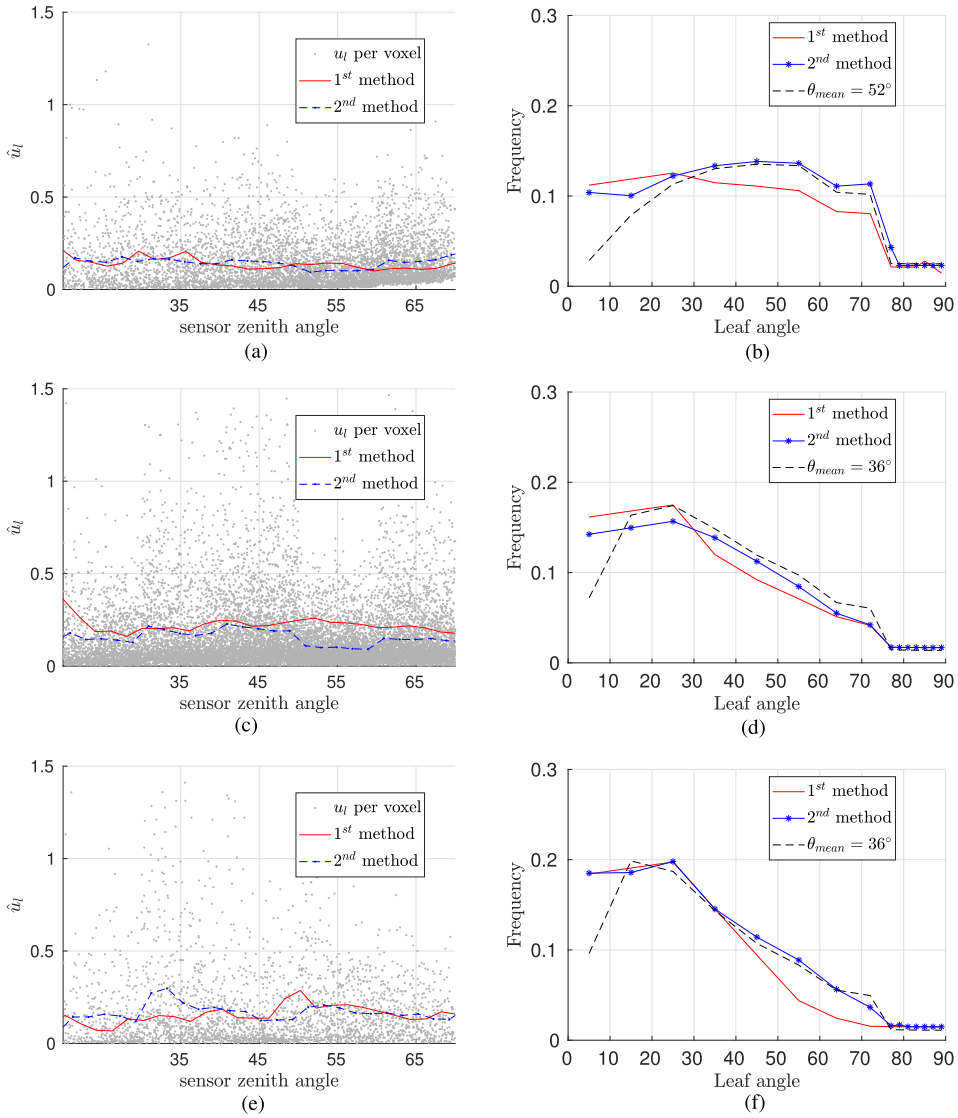

Fig. 16. Estimation of u_l and LAD of actual TLS data using traditional and novel technique. Dashed curves in the second column are the closest spherical distributions to the novel technique, θ_{mean} is the average of leaf angle.

in the various forest stands. Comparison between u_l estimation considering both techniques demonstrates acceptable results in terms of $\overline{u}_l$ stability as a function of the sensor elevation. Nevertheless, the novel technique shows better performances in this sense. For instance, for the Birch stand, the traditional technique presents a significant decrease of $\overline{u}_l$ at small inclinations compared to the remain points of the curves. In terms of LAD, the two methods give relatively similar distribution and based on θ_{mean} values it is possible to say roughly that pine, spruce, and birch LAD are planophile, spherical, and planophile, respectively.

To show the distribution of the estimated 3-D foliage density using actual TLS data, an example of the estimated u_l values are shown in Fig. 17, which illustrates a 3-D visualization of the estimated u_l values for an area of the Birch stand. The black points, which correspond to tree trunks, are not included in u_l retrieval. Crowns can be distinguished even though the trees are too close.

u_l assessment actually leads to LAI derivation of the above-mentioned stands. LAI can be calculated as the sum of all the leaf area per voxel of the scene divided by the scene surface. Table X summarizes the LAI and LIDFs values estimated from the different forest stands using both techniques and the actual manually measured LAI and LIDF for each stands [32]. The results of the LAI calculation are very close to the actual ones, and the results of the novel techniques are more accurate.

Concerning the LAD derivation, our result for Birch confirms the one found in [37] when inspecting the same Birch stand and using a high density point cloud of TLS hits. The Pine and Spruce stands were not validated by ground measurements, but results seems to be correct and close to reality as confirmed by other researchers affirming that in general, for temperate and broadleaf forest, possible leaf orientation measurement are planophile, spherical, or plagiophile [25], [38].

3) Comparative Analysis of LAI Accuracy: To evaluate the performances of our developed approach, it is compared to the

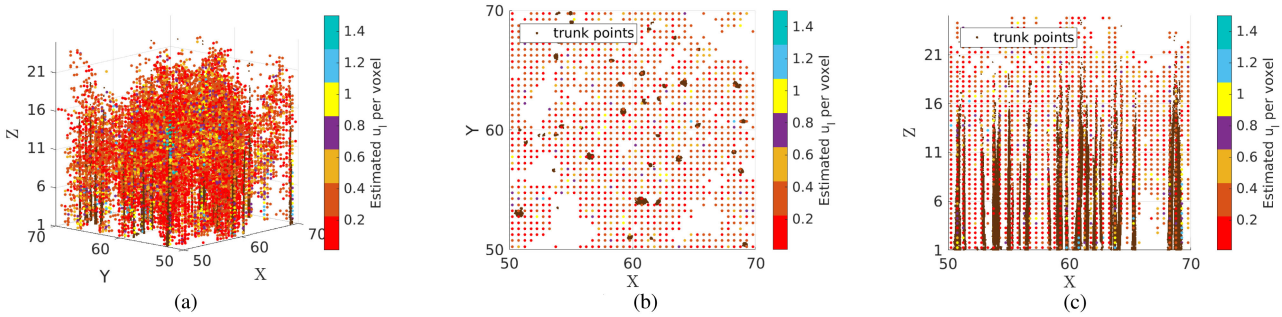

Fig. 17. 3-D visualization of the estimated u_l of an area (20 m × 20 m) from the Birch stand. Trunk point cloud is represented by black dots, while the other dots show the estimated u_l values inside each voxel.

TABLE X
LAI AND LAD ESTIMATION RESULTS OF ACTUAL TLS DATA

	Actual LAI	Estimated LAI		Actual LIDF	Estimated LiDF	
		1^{st} method	2^{nd} method		1^{st} method	2^{nd} method
Spruce	4.36	4.67	4.29	–	Planophile	Planophile
Birch	3.93	3.54	3.99	Planophile	Planophile	Planophile
Pine	1.86	2.03	1.81	–	Spherical	Spherical

TABLE XI
RESULTS AND PERFORMANCES OF LAI MEASUREMENTS DERIVED FROM THE GROUND TRUTH, THE BASELINE TECHNIQUE, AND OUR PROPOSED APPROACH FOR THE THREE FOREST STANDS

	Actual LAI	Baseline technique	Proposed approach	
			1^{st} method	2^{nd} method
Spruce	4.36	6.30	4.67	4.29
Birch	3.93	5.71	3.54	3.99
Pine	1.86	2.17	2.03	1.81
$RMSE_{LAI}$	-	2.6511	0.5264	0.1049

method proposed in [29], which assumes a commonly used LAD, the spherical LIDF, to derive LAI/u_l from TLS data using the Beer Lambert law.

In our study, LAI/u_l derived from the baseline is based on the traditional technique, taken into account all the abovementioned parameters. This study is regarded as a baseline against which we compare our findings. The concern here is whether the spherical LIDF is a valid assumption for estimating LAI using TLS data. Table XI shows the actual LAI as well as the results and performances of the LAI estimation from the baseline (i.e., assuming a spherical LAD) and from our proposed joint estimation approach using both traditional and novel techniques. Estimated LAI values from our both retrieval techniques agree with the actual LAI values better than the baseline case, which overestimates LAI with high RMSE_{LAI} (2.65).

To summarize, adopting a spherical LAD leads to biased LAI estimates, proving that this assumption is inaccurate to derive LAI using TLS point cloud for our stands. Our proposed approach exhibiting the influence of LAD on transmittance assessment, and therefore, on LAI retrieval demonstrating the nongeneral validity of spherical distribution that is traditionally assumed when no actual leaf inclination angle measurements are available.

VI. DISCUSSION

TLS proves to be an efficient method for quantifying LAD and u_l due to its ability to acquire 3-D data with possibility to make distinction between foliage and woody materials. Quantification of specific LAD in a stand has a potential to increase different foliage properties retrieval accuracy such as u_l and LAI. The spherical distribution is the most widely used due to its simplicity in calculating the G-function (approximated to 0.5 in any direction) [39], but such simplification fails to consider the variation of LAD. In reality, LAD could vary for a given tree type as a function of the stand age [28]. This points out the relevance of LAD estimation.

The accuracy of the estimation results is closely associated with the exact approximation of the number of total TLS rays reaching each voxel. In our case, they are first derived per solid angle based on the triangulation of the sphere containing the

point cloud and including regularization hypothesis to reduce the impact of the canopy heterogeneity effect.

u_l curves in the first set of simulated data relative to homogeneous case are not very smooth due to the low number of voxels over the sensor zenith angle interval of 2°. Applying our approach on larger scenes allows us to reach better performances as it leads to the increase of this number and, therefore, decrease uncertainty. This is well shown in comparison between homogeneous and heterogeneous cases. Indeed, despite the heterogeneity in the latter case it provides the best results due to the increase of the scene size.

It should be highlighted that compared to TLS data scanned from actual forests, the simulation data have less noisy points, and well known spatial distribution. Nevertheless, that does not prevent the LAD retrieval in actual case.

Compared to other previously validated methods for the retrieval of LAD information with TLS data, for example, in [27] and [40], LAD retrieval was carried out with smaller isolated trees or shrubs with TLS located close to the targets. Here, we are demonstrating the potential challenge of TLS calculation techniques for the retrieval of LAD information for large tree size (30 m height) and long distances.

Laser scanning data are perfectly built to acquire point cloud to assess 3-D tree structure information. Although the ALS signal has the capacity to reach the ground through open or sparse canopies, in most cases the bottom and inner crown sections were not detected by such a sensor, as the laser pulses were mainly returned by the upper part of the crown. While TLS may provide more detailed data on the lower canopy part. This complementarity has led to a growing interest in the use of TLS to complement the strengths of ALS.

VII. Conclusion

In this work, we proposed a new approach to u_l and LAD joint estimation of a vegetation scene using TLS data. For a comprehensive study of the relationship between light transmittance and forest structure, a forward ray tracing model was developed to simulate TLS observation inside vegetation scenes with different complexity degrees. Then, an inverse model was developed in order to retrieve u_l and LAD using traditional technique and a new one allowing us to take into account the ray traveling distance variation in each voxel. The obtained results over simulated data show high performances for both homogeneous and heterogeneous canopies. Our findings revealed that our estimates were considerably close to the actual u_l and LIDF values with (Biais$_{u_l} \in [0.001\ 0.006]$, RMSE$_{u_l} \in [0.019\ 0.045]$, RMSE$_{\text{LIDF}} \in [0.019\ 0.038]$) for homogeneous dataset and (Biais$_{u_l} \in [0.001\ 0.045]$, RMSE$_{u_l} \in [0.03\ 0.079]$, RMSE$_{\text{LIDF}} \in [0.011\ 0.018]$) for heterogeneous dataset with different tree crown geometries (i.e., conical and elliptical). The accuracy of LAI estimations for actual TLS, with the traditional and novel techniques, RMSE$_{\text{LAI}}$ was 0.526 and 0.1049, respectively. Besides, our results outperform the RMSE$_{\text{LAI}}$ of the baseline technique (2.651). Future studies may investigate the effect of the laser beam divergence on u_l estimates because in actual sensor configuration the laser footprint have not a null-size and taking into consideration in the inversion technique would increase the performances. Besides, results accuracy could be improved using different TLS data obtained from multiple scanning positions of the studied vegetation scene.

Appendix A
SCE-UA Algorithm

Algorithm 1: Complex Algorithm.

Initialize N set of solutions $\{P_l^1, P_l^2, ..., P_l^N\}$;
Calculate cost functions $c(P_l^1), c(P_l^2), ..., c(P_l^N)$;
Sort $\{c(P_l^j)\}_{j=1,...,N}$ increasingly;
Distribution of the solutions into complexes $\{C_h\}_{h=1,...,p}$;
repeat
  for $h = 1 : p$ **do**
    Evolve C_h using the Simplex (Algorithm 2);
  Merge $\{C_h\}_{h=1,...,p}$;
  Sorting and redistribution into complexes $\{C_h\}_{h=1,...,p}$;
until *Convergence Criteria*;

Appendix B
Simplex Algorithm

Algorithm 2: Simplex Algorithm.

Sort the m solutions of C according to their cost $c_1 \leq c_2 \leq ... \leq c_m$;
Calculate the centroid of the $m-1$ first solutions: $g \leftarrow \dfrac{\sum_{i=1}^{m-1} P_{l_i}^j}{m-1}$;
Reflection of P_l^m with respect to g: $r \leftarrow g - P_l^m$;
if $c(r) <= c(P_l^m)$ **then**
  extension coefficient calculation: $e \leftarrow 3g - 2P_l^m$;
  if $c(e) <= c(r)$ **then**
    $P_l^m \leftarrow e$ and $c(P_l^m) \leftarrow c(e)$;
else
  contraction coefficients calculation $t \leftarrow \dfrac{g + P_l^m}{2}$ and $t_2 \leftarrow \dfrac{g + r}{2}$;
  if $c(t_2) < c(t)$ **then**
    $P_l^m \leftarrow t_2$ and $c(P_l^m) \leftarrow c(t_2)$;
  if $c(t) < c(P_l^m)$ **then**
    $P_l^m \leftarrow t$ and $c(P_l^m) \leftarrow c(t)$;
  else
    Shrink the Simplex where $\{P_l^i, i \in \{2, .., m\}\}$ is transformed to the half of path from P_l^1, $P_l^i \leftarrow \dfrac{P_l^i + P_l^1}{2}$ and $c(P_l^i)$ is updated.;

ACKNOWLEDGMENT

The authors would like to thank Prof. A. Kuusk for providing us the actual TLS data of Estonian forest.

REFERENCES

[1] R. Seidl *et al.*, "Forest disturbances under climate change," *Nature Climate Change*, vol. 7, no. 6, pp. 395–402, 2017.
[2] D. Baldocchi and P. Harley, "Scaling carbon dioxide and water vapour exchange from leaf to canopy in a deciduous forest. II Model testing and application," *Plant, Cell Environ.*, vol. 18, no. 10, pp. 1157–1173, 1995.
[3] B. Kötz, "Estimating biophysical and biochemical properties over heterogeneous vegetation canopies: Radiative transfer modeling in forest canopies based on imaging spectrometry and LiDAR," Ph.D. dissertation, Dept. Geography, Remote Sensing Laboratories, Univ. Zurich, Zurich, Switzerland, 2006.
[4] G. Asrar, M. Fuchs, E. Kanemasu, and J. Hatfield, "Estimating absorbed photosynthetic radiation and leaf area index from spectral reflectance in wheat 1," *Agronomy J.*, vol. 76, no. 2, pp. 300–306, 1984.
[5] C. Emmel *et al.*, "Canopy photosynthesis of six major arable crops is enhanced under diffuse light due to canopy architecture," *Glob. Change Biol.*, vol. 26, no. 9, pp. 5164–5177, 2020.
[6] S. Hill, H. Latifi, M. Heurich, and J. Müller, "Individual-tree-and stand-based development following natural disturbance in a heterogeneously structured forest: A lidar-based approach," *Ecological Informat.*, vol. 38, pp. 12–25, 2017.
[7] M. Bouvier, S. Durrieu, R. A. Fournier, and J.-P. Renaud, "Generalizing predictive models of forest inventory attributes using an area-based approach with airborne LiDAR data," *Remote Sens. Environ.*, vol. 156, pp. 322–334, 2015.
[8] I. Jonckheere *et al.*, "Review of methods for in situ leaf area index determination: Part I. Theories, sensors and hemispherical photography," *Agricultural Forest Meteorol.*, vol. 121, no. 1/2, pp. 19–35, 2004.
[9] M. Weiss, F. Baret, G. Smith, I. Jonckheere, and P. Coppin, "Review of methods for in situ leaf area index (LAI) determination: Part II estimation of LAI, errors and sampling," *Agricultural Forest Meteorol.*, vol. 121, no. 1/2, pp. 37–53, 2004.
[10] K. Calders, I. Jonckheere, J. Nightingale, and M. Vastaranta, *Remote Sensing Technology Applications in Forestry and REDD+*. Basel, Switzerland: MDPI, 2020.
[11] M. A. Wulder *et al.*, "LiDAR sampling for large-area forest characterization: A review," *Remote Sens. Environ.*, vol. 121, pp. 196–209, 2012.
[12] M. Beland *et al.*, "On promoting the use of LiDAR systems in forest ecosystem research," *Forest Ecol. Manage.*, vol. 450, 2019, Art. no. 117484.
[13] J. Frey, B. Joa, U. Schraml, and B. Koch, "Same viewpoint different perspectives—A comparison of expert ratings with a TLS derived forest stand structural complexity index," *Remote Sens.*, vol. 11, no. 9, 2019, Art. no. 1137.
[14] X. Liang, J. Hyyppä, A. Kukko, H. Kaartinen, A. Jaakkola, and X. Yu, "The use of a mobile laser scanning system for mapping large forest plots," *IEEE Geosci. Remote Sens. Lett.*, vol. 11, no. 9, pp. 1504–1508, Sep. 2014.
[15] J. Shao *et al.*, "Single scanner BLS system for forest plot mapping," *IEEE Trans. Geosci. Remote Sens.*, vol. 59, no. 2, pp. 1675–1685, Feb. 2021.
[16] Y. Chen *et al.*, "Rapid urban roadside tree inventory using a mobile laser scanning system," *IEEE J. Sel. Topics Appl. Earth Observ. Remote Sens.*, vol. 12, no. 9, pp. 3690–3700, Sep. 2019.
[17] A. Kuusk, M. Lang, S. Märdla, and J. Pisek, "Tree stems from terrestrial laser scanner measurements," *Forestry Stud.*, vol. 63, no. 1, pp. 44–55, 2015.
[18] E. Grau, S. Durrieu, R. Fournier, J.-P. Gastellu-Etchegorry, and T. Yin, "Estimation of 3D vegetation density with terrestrial laser scanning data using voxels. A sensitivity analysis of influencing parameters," *Remote Sens. Environ.*, vol. 191, pp. 373–388, 2017.
[19] X. Zhu *et al.*, "Improving leaf area index (LAI) estimation by correcting for clumping and woody effects using terrestrial laser scanning," *Agricultural Forest Meteorol.*, vol. 263, pp. 276–286, 2018.
[20] G. Yan *et al.*, "Review of indirect optical measurements of leaf area index: Recent advances, challenges, and perspectives," *Agricultural Forest Meteorol.*, vol. 265, pp. 390–411, 2019.
[21] I. Indirabai, M. H. Nair, J. R. Nair, and R. R. Nidamanuri, "Direct estimation of leaf area index of tropical forests using LiDAR point cloud," *Remote Sens. Appl., Soc. Environ.*, vol. 18, 2020, Art. no. 100295.
[22] Y. Bao, W. Ni, D. Wang, C. Yue, H. He, and H. Verbeeck, "Effects of tree trunks on estimation of clumping index and LAI from hemiview and terrestrial LiDAR," *Forests*, vol. 9, no. 3, 2018, Art. no. 144.
[23] A. Kuusk, J. Pisek, M. Lang, and S. Märdla, "Estimation of gap fraction and foliage clumping in forest canopies," *Remote Sens.*, vol. 10, no. 7, 2018, Art. no. 1153.
[24] J. M. Norman and G. S. Campbell, "Canopy structure," in *Plant Physiological Ecology*. Berlin, Germany: Springer, 1989, pp. 301–325.
[25] J. Pisek, O. Sonnentag, A. D. Richardson, and M. Mõttus, "Is the spherical leaf inclination angle distribution a valid assumption for temperate and boreal broadleaf tree species?," *Agricultural Forest Meteorol.*, vol. 169, pp. 186–194, 2013.
[26] S. Jin, M. Tamura, and J. Susaki, "A new approach to retrieve leaf normal distribution using terrestrial laser scanners," *J. Forestry Res.*, vol. 27, no. 3, pp. 631–638, 2016.
[27] G. Zheng and L. M. Moskal, "Leaf orientation retrieval from terrestrial laser scanning (TLS) data," *IEEE Trans. Geosci. Remote Sens.*, vol. 50, no. 10, pp. 3970–3979, Oct. 2012.
[28] J. Liu *et al.*, "Variation of leaf angle distribution quantified by terrestrial LiDAR in natural European beech forest," *ISPRS J. Photogrammetry Remote Sens.*, vol. 148, pp. 208–220, 2019.
[29] G. Zheng, L. M. Moskal, and S.-H. Kim, "Retrieval of effective leaf area index in heterogeneous forests with terrestrial laser scanning," *IEEE Trans. Geosci. Remote Sens.*, vol. 51, no. 2, pp. 777–786, Feb. 2013.
[30] W. Verhoef, "Light scattering by leaf layers with application to canopy reflectance modeling: The sail model," *Remote Sens. Environ.*, vol. 16, no. 2, pp. 125–141, 1984.
[31] A. Kuusk, M. Lang, and T. Nilson, "Forest test site at Järvselja, Estonia," in *Proc. 3rd Workshop CHRIS/Proba*, Frascati, Italy, 2005, pp. 21–23.
[32] A. Kuusk, M. Lang, and J. Kuusk, "Database of optical and structural data for the validation of forest radiative transfer models," in *Light Scattering Reviews* 7. Berlin, Germany: Springer, 2018, pp. 109–148.
[33] Q. Duan, S. Sorooshian, and V. K. Gupta, "Optimal use of the SCE-UA global optimization method for calibrating watershed models," *J. Hydrol.*, vol. 158, no. 3/4, pp. 265–284, 1994.
[34] Q. Duan, S. Sorooshian, and V. Gupta, "Effective and efficient global optimization for conceptual rainfall-runoff models," *Water Resour. Res.*, vol. 28, no. 4, pp. 1015–1031, 1992.
[35] J. A. Nelder and R. Mead, "A simplex method for function minimization," *Comput. J.*, vol. 7, no. 4, pp. 308–313, 1965.
[36] Q. Duan, V. K. Gupta, and S. Sorooshian, "Shuffled complex evolution approach for effective and efficient global minimization," *J. Optim. Theory Appl.*, vol. 76, no. 3, pp. 501–521, 1993.
[37] A. Kuusk, "Leaf orientation measurement in a mixed hemiboreal broadleaf forest stand using terrestrial laser scanner," *Trees*, vol. 34, pp. 1–10, 2019.
[38] P. Oker-Blom and S. Kellomäki, "Effect of angular distribution of foliage on light absorption and photosynthesis in the plant canopy: Theoretical computations," *Agricultural Meteorol.*, vol. 26, no. 2, pp. 105–116, 1982.
[39] C. T. de Wit, "Photosynthesis of leaf canopies," Pudoc, La Union, Philippines, Tech. Rep., 1965.
[40] B. N. Bailey and W. F. Mahaffee, "Rapid measurement of the three-dimensional distribution of leaf orientation and the leaf angle probability density function using terrestrial LiDAR scanning," *Remote Sens. Environ.*, vol. 194, pp. 63–76, 2017.

Ameni Mkaouar received the Engineering degree in networks and telecommunication from the National School of Electronics and Telecommunications of Sfax, Sfax, Tunisia, in 2017. She is currently working toward the Ph.D. degree in computer systems engineering with the National Engineering School of Sfax, Sfax, Tunisia.

She is currently a Student Researcher with the Digital Research Centre of Sfax, Sfax, Tunisia. Her main research interest include forest structure study using LiDAR point cloud processing.

Abdelaziz Kallel received the Engineering and M.S. degrees in telecommunications from the Higher School of Communication of Tunis, Aryanah, Tunisia, in 2003 and 2004, respectively, the Ph.D. degree in physics from Paris-Sud University, Orsay, France, in 2007, and the HDR degree in remote sensing image physical and statistical modeling and processing from the University of Sfax, Sfax, Tunisia, in 2014.

He was a Postdoctoral Scientist with the Laboratory of Climate and Environmental Sciences, SaintAubin, France, and Tartu Observatory, Tõravere, Estonia, in 2008 and 2009, respectively. He is currently a Senior Researcher of Remote Sensing with the Digital Research Centre of Sfax, Sakiet Ezzit, Tunisia. Particularly, he is the Head of the Remote Sensing for Smart Agriculture Team as well as the Laboratory of Signals, Systems, Artificial Intelligence and Networks. His research interests include radiative transfer theory and application to vegetation cover property inversion using passive and active optical remote sensing techniques.

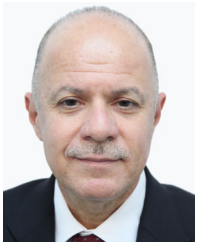

Zouhaier Ben Rabah received the Engineering and M.S. degrees in telecoms from Sup'Com, Aryanah, Tunisia, in 2003 and 2004, and the Ph.D. degree in remote sensing, signal processing from the Telcom Bretagne, Brest, France, in 2011.

He was an Assistant Professor with Military Academy, Tunisia, in 2015 and 2016, respectively. He is currently a Senior Researcher of Remote Sensing with the National Center of Mapping and Remote Sensing, Tunisia, particularly and he is the head of the team Remote Sensing for soil science. He is interesting to digital soil mapping and Tunisian soil library development.

Thouraya Sahli Chahed received the Engineering and M.S. degrees in rural engineering from the National Agronomic Institute of Tunis, Tunis, Tunisia, in 1990 and 1992.

She was an Assistant Technologist with the Higher Institute of Technological Studies, Nabeul, Tunisia, from 2003 to 2009. She has been a member of the Tunisian delegation to sessions of the United Nations Committee for the Peaceful Use of Outer Space (COPUOS) and its subcommittees since 2010. She is currently the responsible of the space activities development service in the National Center of Mapping and Remote Sensing, Tunisia. Her research interests include to earth observation and mapping using remote sensing techniques.